J. Fluid Mech. (2014), *vol.* 742, *pp* 119–151. © Cambridge University Press 2014
doi:10.1017/jfm.2013.641

The turbulent/non-turbulent interface and entrainment in a boundary layer

Kapil Chauhan†, Jimmy Philip, Charitha M. de Silva, Nicholas Hutchins and Ivan Marusic

Department of Mechanical Engineering, The University of Melbourne, Parkville, VIC 3010, Australia

(Received 1 May 2013; revised 15 October 2013; accepted 2 December 2013;
first published online 21 February 2014)

The turbulent/non-turbulent interface in a zero-pressure-gradient turbulent boundary layer at high Reynolds number ($Re_\tau = 14\,500$) is examined using particle image velocimetry. An experimental set-up is utilized that employs multiple high-resolution cameras to capture a large field of view that extends $2\delta \times 1.1\delta$ in the streamwise/wall-normal plane with an unprecedented dynamic range. The interface is detected using a criteria of local turbulent kinetic energy and proves to be an effective method for boundary layers. The presence of a turbulent/non-turbulent superlayer is corroborated by the presence of a jump for the conditionally averaged streamwise velocity across the interface. The steep change in velocity is accompanied by a discontinuity in vorticity and a sharp rise in the Reynolds shear stress. The conditional statistics at the interface are in quantitative agreement with the superlayer equations outlined by Reynolds (*J. Fluid Mech.*, vol. 54, 1972, pp. 481–488). Further analysis introduces the mass flux as a physically relevant parameter that provides a direct quantitative insight into the entrainment. Consistency of this approach is first established via the equality of mean entrainment calculations obtained using three different methods, namely, conditional, instantaneous and mean equations of motion. By means of 'mass-flux spectra' it is shown that the boundary-layer entrainment is characterized by two distinctive length scales which appear to be associated with a two-stage entrainment process and have a substantial scale separation.

Key words: intermittency, turbulent boundary layers, turbulent flows

1. Introduction

The spreading of a turbulent flow into non-turbulent flow via the process of entraining the non-turbulent fluid into the turbulent region is not only relevant for technological applications but is also theoretically intriguing. The turbulent/non-turbulent interface (TNTI) refers to the specific case of mixing where one fluid is characterized by the presence of turbulence while the other is characterized by its absence. The term interface has been loosely used to describe the region where dynamical processes are responsible for the conversion of a non-turbulent flow to a turbulent state and as such the TNTI is considered as the surface that demarcates the turbulent flow from the non-turbulent flow. The term entrainment encompasses all mechanisms that are responsible for the transfer of mass across the interface.

† Email address for correspondence: kchauhan@unimelb.edu.au

https://doi.org/10.1017/jfm.2013.641 Published online by Cambridge University Press

The entrainment mechanisms do not necessarily act at the interface itself and can precede the interface dynamics; e.g. there exists an induced inflow in the case of a jet/plume (laminar or turbulent) (e.g. Taylor 1958; Schneider 1981). This induced velocity is zero in boundary layers and wakes (Hunt 1994). Following Turner (1986), we consider the mean entrainment velocity as the rate at which external fluid flows into the turbulent flow across the mean interface in the laboratory frame of reference. The mean interface velocity is the rate at which the edge of the turbulent flow is spreading out, e.g. the growth in thickness δ or half-height b in boundary layers and jets, respectively. While the mean entrainment dynamics are examined in the fixed laboratory frame of reference, instantaneously the local entrainment velocity is considered as the velocity of fluid relative to the transient TNTI (further discussed in § 7). The entrainment velocity can also be defined based on the flux of concentration or temperature (Hunt, Rottman & Britter 1984) in flows where the interface is characterized by spread of a scalar (e.g. Westerweel *et al.* 2009). For the case of entrainment in homogeneous fluids (in contrast to flows with large density differences or stable stratification, see Turner (1986)) two scenarios emerge: one, where turbulence is created and the flow has no mean or bulk shear; and two, where the turbulence can be maintained by a mean shear, such as in jets, wakes and boundary-layer flows. It seems more plausible that the mechanisms involved in the spreading of the turbulent region and entrainment of the non-turbulent fluid into the turbulent core are different in both cases. In the first case, due to the absence of the mean shear for the production of turbulence, either the turbulence decays (as in grid-generated turbulence), or the turbulence has to be continuously maintained by constant agitation at a boundary (such as employing an oscillating grid, see e.g. Holzner *et al.* (2007)). These are more akin to the turbulent diffusion process (introduced by Taylor 1921). In the second case, since the flows have been observed to be dominated by large-scale motions (such as those observed in jets by Brown & Roshko (1974) and in wakes by Cannon, Champagne & Glezer (1993), to name a few), it is not clear how important the turbulent diffusion is compared with the role of large-scale motions. This leads to important questions regarding the roles played by the large-scale, predominantly inviscid motions and those by the small-scale, diffusive and primarily viscous motions.

In the seminal work of Corrsin & Kistler (1955), two important hypotheses are made: one, that there is a step change in velocity across the TNTI; and two, that the spreading process of the turbulent region in shear flows is similar to turbulent diffusion (gauged by the observation of wake shadowgraphs, which unfortunately do not show the entrapped non-turbulent fluid inside the turbulent region, as mentioned by Townsend (1976)). After the initial dismay at not finding a velocity jump across the interface in the 1970s (in boundary-layer flows by Kovasznay, Kibens & Blackwelder 1970), more recently it has been observed that, indeed, there does exist a velocity jump at the TNTI of boundary layers (Semin *et al.* 2011) and in wakes and jets, though over a small but finite region (Bisset, Hunt & Rogers 2002; Westerweel *et al.* 2005). Regarding the second hypothesis of spreading by turbulent diffusion, it is uncertain whether it is fully correct. If so, it would imply that the large-scale motions have no role to play in the spreading, which is highly unlikely considering that bulk motion is sufficient to determine the spreading and entrainment in shear flows (Townsend 1966). A reconciliation of the large-scale and small-scale points of view towards entrainment is to some extent provided by Sreenivasan and coworkers (e.g. Sreenivasan, Ramshankar & Meneveau 1989) by showing than an extensive surface area is created by the large-scale motions such that the total entrainment is

https://doi.org/10.1017/jfm.2013.641 Published online by Cambridge University Press

independent of viscosity (or Reynolds number), even though the actual conversion of non-turbulent fluid to turbulent is carried out by the small-scale viscous action at Kolmogorov scales.

There is a general consensus that the entrainment from a large-scale perspective is different for different flows, however, it is not yet clear whether the entrainment process is similar for all flows if viewed from a small scale, even though one would tend to presume so. Philip & Marusic (2012) suggested that the large-scale contributions could be divided into two major components: the radial inflow of irrotational fluid (such as in jets) and the engulfing motion (present in all shear flows). Accordingly, shear flows for the purpose of studies in entrainment can be differentiated into three major categories (Philip & Marusic 2012): (i) jets (where there is a radial inflow, along with large-scale 'engulfment', see Mathew & Basu (2002) and Westerweel *et al.* (2009)); (ii) wakes as well as boundary-layer flows (where the large scales are only involved in the engulfing motion, see Bisset *et al.* (2002)); and (iii) the oscillating-grid experiment (where no large-scale effects are involved, see Holzner & Lüthi (2011)). Accordingly, the overall entrainment is envisaged to be such that the non-turbulent fluid is brought into contact with the turbulent interface via large-scale motions, and this non-turbulent fluid in turn is converted into turbulent motions by the small-scale eddies. We should mention here that the term 'engulfment' is more often used to imply a 'blob' of non-turbulent fluid entrapped in turbulent fluid, such as 'an amoeba ingests food' (Kovasznay 1967). We consider engulfment as a rate-determining inviscid first stage in which large packets of non-turbulent fluid are drawn into the turbulent region, while small-scale viscous processes at the interface are denoted as nibbling (Mathew & Basu 2002; Holzner *et al.* 2007). In recent literature this view point has been commonly held (e.g. Westerweel *et al.* 2005; da Silva & Pereira 2008). Accordingly, we shall attribute the action of large scales as engulfment and the action of small scales as nibbling.

With the exception of the present study and that of Semin *et al.* (2011) the understanding of TNTI characteristics in boundary layers is still largely based on the classical studies in the 1960s and 1970s. As our emphasis in this paper is on the turbulent boundary layer, only the relevant previous work is introduced to the reader. The earliest effort to quantify the rate of entrainment in a boundary layer is by Head (1958) in the mean form. The non-dimensional average rate of entrainment of fluid into the turbulent boundary layer could be specified as a function of the mean velocity profile (Thompson 1964). The analysis of Head (1958) and Thompson (1964) represents a small subset of the concurrent research at the time to predict the development of a turbulent boundary layer under various external conditions (Coles & Hirst 1968). Subsequent studies focused on the mechanisms of entrainment which on an instantaneous sense were either considered as small-scale phenomena (Corrsin & Kistler 1955) or a large-scale instability mechanism (Townsend 1966). Fiedler & Head (1966) utilized smoke visualization along with hotwire and Pitot tube measurements to conclude that the mean intermittency distribution is dependent on the streamwise pressure gradient but not the Reynolds number. Kovasznay (1970) forwarded the understanding that large-scale turbulent bursts that emerge from near the wall survive long enough to reach the outer part of the boundary layer resulting in the external intermittency characterized by turbulent/non-turbulent regions. The strong correlation between the large-scale motions near the wall and the shape and motion of the TNTI is demonstrated by Kovasznay *et al.* (1970). They conjectured the existence of a whole reverse cascade of eddies, beginning with more frequent and small-scale bursts near the wall. These small-scale eddies grow or merge into

https://doi.org/10.1017/jfm.2013.641 Published online by Cambridge University Press

larger scales and eventually reach the non-turbulent flow at a lesser frequency than their origin. These views are consistent with the views of Adrian (2007) where the bulges/valleys in the outer region are interpreted as large-scale motions in the form of packets of attached eddies that extend to the edge of the boundary layer. However, it is noted that the large-scale bulges in outer region could also be a consequence of an instability mechanism (Townsend 1966).

Nychas, Hershey & Brodkey (1973) by visualization showed the occurrence of transverse vortices and suggested that they are one of the mechanisms that induce higher-speed fluid towards the inner zones. The characteristics of the leading and trailing edges of the turbulent bulges in the outer part of the boundary layer are examined by Hedley & Keffer (1974*a*). They found that sharp changes occur through the 'backs', i.e. the TNTI when one moves from the turbulent zone to the non-turbulent zone in the direction opposite to the flow. On the other hand the 'fronts' exhibit a more diffusive behaviour in their analysis. Chen & Blackwelder (1978) used temperature as a passive contaminant in order to study the large-scale structure in the outer part. They confirmed the presence of a sharp interface by conditional averages of temperature profiles. Mean intermittency measurements using concentration sources from two different elevations in the boundary layer were performed by Fackrell & Robins (1982) while intermittency characteristics under different free-stream turbulence levels are documented by Hancock & Bradshaw (1989). Most of these studies are at relatively low Reynolds numbers and lacked comprehensive measurement apparatus to track the instantaneous TNTI in two dimensions.

Accordingly, there are two main objectives of the present work. First, to quantify the interface properties (particularly the velocity jump across it) in the turbulent boundary layer at a relatively high Reynolds number and discuss its implications. Since similar studies do exist for wakes and jet, the present study will provide insight for the boundary-layer flow and complete the list by including the wall-shear flow. Second, to understand the entrainment of the fluid across the interface from the large-scale and small-scale points of view. To this end, we shall calculate mass entrainment using three methods and also introduce the 'mass-flux spectra' to differentiate the length scales involved in the entrainment.

The outline of the paper is as follows: § 2 describes the experimental setup and the particle image velocimetry (PIV) measurements at high Reynolds number; § 3 describes the procedure to determine the interface using velocity data from PIV in a turbulent boundary layer; § 4 provides the spatial statistics of the interface; the conditionally averaged statistics relative to the interface location are presented in § 5; the instantaneous and mean mass flux across the interface and its relevant length scales are examined in § 7; a summary and conclusions are included in § 8. The notation adopted is as follows. The streamwise and wall-normal axes are represented by x and z, respectively, in the Cartesian system. The distance along the interface is s (see figure 1*a*). The instantaneous streamwise velocity, wall-normal velocity and spanwise vorticity are represented by $\tilde{U}$, $\tilde{W}$ and $\tilde{\Omega}_y$, respectively. The corresponding mean components are denoted as U, W and Ω_y and lowercase symbols are used for fluctuating components (u, w and ω_y). The superscript '+' indicates the scaling by inner length (ν/u_τ) and velocity (u_τ) scales, where ν and u_τ are the kinematic viscosity and friction velocity, respectively. The subscript 'i' denotes quantities at the interface. Further notation for the conditional averages and mass flux will be introduced in the relevant sections.

https://doi.org/10.1017/jfm.2013.641 Published online by Cambridge University Press

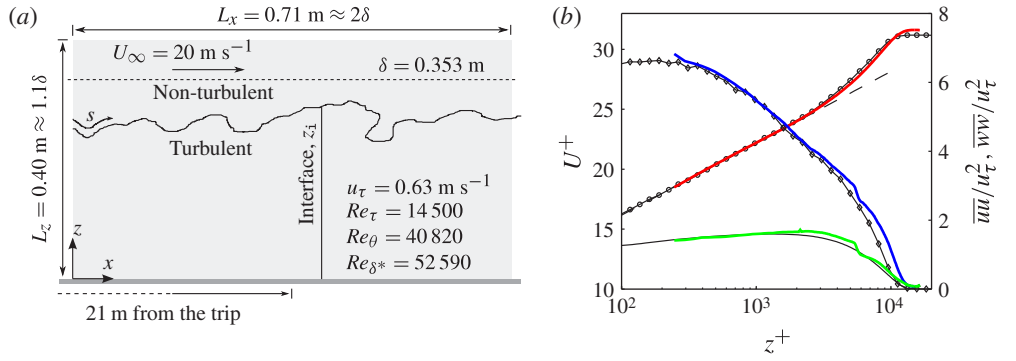


FIGURE 1. (Colour online) (*a*) Schematic of the flow and PIV measurement configuration. The shaded rectangle indicates the composite field of view from eight cameras. (*b*) Profiles for mean statistics: solid coloured curves, present PIV data; dashed line, log-law $1/0.384\ln(z^+) + 4.17$; ∘, U^+; ⋄, $\overline{uu}$, hotwire data at $Re_\tau = 13\,200$ (Hutchins *et al.* 2009); solid (black) line, $\overline{ww}$ formulation of Marusic & Kunkel (2003).

2. Measurement details

Two-component PIV measurements over a two-dimensional plane are performed in the high-Reynolds-number boundary-layer wind tunnel (HRNBLWT) at the University of Melbourne's Walter Bassett Aerodynamics Laboratory. The tunnel has a 27 m long test section resulting in a thick turbulent boundary layer (≈0.37 m) towards the end of the section. This makes it possible to examine the flow with relatively high spatial resolution. In a flow with large characteristic length scale, such as the present experiment, conventional PIV is sufficient to capture small-scale flow features (of the order of Kolmogorov scale η) with good magnification, while the large scales are often not fully captured. However, current imaging and optical infrastructure limits the field of view to a small subsize of the boundary-layer height in a thick boundary layer. Hence, it is challenging to measure the full dynamic range of motions in a high-Reynolds-number flow where a large scale separation exists between the smallest and the largest length scales (e.g. δ/η is approximately $O(10^3)$ near the edge of a turbulent boundary layer at $Re_\tau = \delta u_\tau/\nu \approx 14\,500$, where δ is the boundary-layer thickness). To overcome this limitation eight cameras are used to obtain a large composite field of view as illustrated in figure 1. The measurements are performed at a streamwise location 21 m downstream from the trip with 20 m s^{-1} free-stream velocity under a zero pressure gradient. The resulting Kármán number for the boundary layer $Re_\tau \approx 14\,500$ and other relevant parameters are presented in figure 1. Also, the Reynolds number based on the Taylor's microscale λ_T is estimated to be approximately 300 near the mean interface location. The boundary-layer thickness (δ) and the friction velocity (u_τ) are determined from the composite velocity fit of Chauhan, Monkewitz & Nagib (2009). The objective for the PIV set-up was to have a field of view that extends beyond the boundary-layer thickness δ with sufficient streamwise extent. To achieve this eight PCO 4000 cameras (4008 × 2672 pixels) are placed in two rows. The bottom cameras are fitted with 180 mm Tamaron Macro lenses and capture the region from the wall up to $z \approx 0.15$ m. The top cameras capture the outer region between 0.1 m up to 0.4 m equipped with 105 mm Sigma Macro lenses. The bottom cameras have a higher magnification than the top cameras which

https://doi.org/10.1017/jfm.2013.641 Published online by Cambridge University Press

is suitable for wall-bounded shear flows where small-scale motions are prominent in the near-wall region. The resulting magnification for the top and bottom cameras are 100 and 60 μm per pixel, respectively. An interrogation window of 24 × 24 pixels is used for the top cameras with 50 % overlap, while the bottom camera used an interrogation window of 16 × 16 pixels. In our measurements the ratio of Taylor microscale (λ_T) to the interrogation window size (Δ_i) is approximately three ($\lambda_T/\Delta_i \approx 3$), while the ratio of interrogation window size to the Kolmogorov scale is approximately six ($\Delta_i/\eta \approx 6$, $\eta \approx 16\nu/u_\tau$ in the outer region). The bottom cameras have the same spacing between vectors as that of the top camera. An overlap of at least 2 cm between cameras in real space ensured that the vector field from each camera is suitably merged. Illumination is achieved by a laser sheet beamed from underneath the glass floor, close to the spanwise centre of the tunnel, using a Spectra Physics 'QuantaRay' Nd:YAG laser rated 400 mJ at 532 nm. A total of 1440 synchronous images are acquired by all eight cameras at 2 Hz. The double-frame images are interrogated using fast Fourier transform (FFT)-based cross-correlation with standard algorithms such as multipass, multigrid and second-order correlation for spurious correction (Hart 2000). After discarding images with poor seeding density and spurious vectors a total of 1250 images are used for the present analysis with 590 × 328 vectors over a streamwise/wall-normal region of $2\delta \times 1.1\delta$. Further details of the experiments can be found in de Silva *et al.* (2012).

The results for the mean statistics are shown in figure 1(*b*) as solid lines for the present study. The mean streamwise velocity U and its variance $\overline{uu}$ are compared with hotwire measurement in the same facility at the nearest Reynolds number. Measurements from PIV are in good agreement with the hotwire for the mean flow. The full logarithmic overlap region is measured. The region below $z^+ = 200$ could not be measured by PIV as meaningful and consistent correlation could not be obtained in this region due to reflection of the laser sheet on the glass wall. The variance of the wall-normal fluctuations $\overline{ww}$ is compared with the similarity formulation of Marusic & Kunkel (2003) at an equivalent Reynolds number and is found to be in good agreement with their formulation. One can also notice a slight discontinuity near $z^+ = 6000$ in the profiles for the variance which is due to marginally different spatial resolution of the top and bottom cameras. Overall we find that the present set of PIV measurements agree well with the previous data and provides converged first and second-order statistics.

3. Interface detection

The approach to detect the TNTI in a flow depends on the technique employed for measuring or observing the flow. In the intermittent region single-point techniques such as hotwire anemometry would measure a velocity time series that is turbulent in certain segments and non-turbulent in the rest. In the turbulent zones the local fluctuations are random and with amplitude much larger than the free-stream turbulence intensity, while in the non-turbulent zone the signal is essentially the free stream. For a velocity signal the turbulent/non-turbulent zones could be identified by adopting a threshold technique, where a detector function is calculated from the magnitude or time/space derivative of the velocity. Hedley & Keffer (1974*b*) has listed various turbulence detector functions for time-series measurements. In spatial techniques such as PIV or planar visualization one obtains information over a two-dimensional plane and the temporal resolution of velocity measurement is typically not sufficient for turbulent flows at high Reynolds numbers. For such

https://doi.org/10.1017/jfm.2013.641 Published online by Cambridge University Press

experiments, conventionally the TNTI is determined either by detecting the scalar concentration in a flow or isolating the rotational flow from the irrotational flow (e.g. Sandham *et al.* 1988; Prasad & Sreenivasan 1989; Bisset *et al.* 2002; Westerweel *et al.* 2009). In the present experiments PIV only provides the velocity information throughout the field of view. The seeding particles are present throughout the region of interest and therefore one cannot detect the instantaneous interface of the flow using particle density (or pixel intensity) as a criteria. Consequently we determine the interface from the velocity information. Typically a threshold on the vorticity magnitude has been utilized to distinguish the irrotational flow from the turbulent regions in jets (Westerweel *et al.* 2005; Khashehchi *et al.* 2013) and wakes (Bisset *et al.* 2002). However, in an experimental turbulent boundary layer the free-stream turbulence intensity is not precisely zero (unlike jets) and hence fixing a threshold vorticity magnitude can be challenging even if there is a slight noise in the velocity measurements. Anand, Boersma & Agrawal (2009) compared four different approaches including a vorticity and a velocity criteria to identify the TNTI (although the velocity criteria they used is different to the present approach). In their study they found that although instantaneously the detected interface differs for different criteria, the conditionally averaged statistics are in acceptable agreement with each other. In the current study the local variance of velocity fluctuations is used to distinguish the turbulent from non-turbulent regions. It will be shown in the forthcoming discussion that for turbulent boundary layers the approach adopted here to find an interface from a two-dimensional vector field is sufficiently effective.

At the interface and over a small region above the interface the streamwise convection velocity can be considered to be approximately U_∞ (e.g. Corrsin & Kistler 1955; Fiedler & Head 1966; Kovasznay *et al.* 1970; Jiménez *et al.* 2010). A local turbulent kinetic energy in the frame of reference moving with U_∞, over a 3×3 grid is then defined as

$$\tilde{k} = 100 \times \frac{1}{9\,U_\infty^2} \sum_{m,n=-1}^{1} [(\tilde{U}_{m,n} - U_\infty)^2 + (\tilde{W}_{m,n})^2]. \tag{3.1}$$

In the region above the interface, $\tilde{k}$ should be nearly the same as the free-stream turbulence intensity ($\overline{uu}/U_\infty^2$) of the tunnel, while below the interface $\tilde{k}$ would increase very rapidly as one approaches the wall. This metric provides a direct physical basis to distinguish between the turbulent regions where the kinetic energy of fluctuations is high from the non-turbulent regions where the kinetic energy of fluctuations is nearly zero. Figure 2(*a*) shows contours of $\ln \tilde{k}$ using (3.1). The kinetic energy $\tilde{k}$ is shown on a logarithmic scale for clarity as it varies from nearly zero in the potential region to 100 at the wall. In the free stream $\tilde{k} \approx 0$ and hence the contours of $\ln \tilde{k}$ uniformly take a large negative value in this region. A rapid rise in $\tilde{k}$ is seen as one approaches the wall. The flow can be then characterized as turbulent beyond a certain threshold for $\tilde{k}$. The kinetic energy also appears to be space filling in the turbulent regions where the contours have a darker shade. In contrast, for a high-Reynolds-number flow, the instantaneous vorticity appears in concentrated volume fractions of the total volume (e.g. see figure 3*a* of Jiménez *et al.* 2010). Furthermore, the instantaneous vorticity is not identically zero in the potential region because of finite free-stream turbulence intensity in experiments and measurement noise. These characteristics favour using the kinetic energy criteria to determine the interface in our study. The implementation of such a criteria is described below.

https://doi.org/10.1017/jfm.2013.641 Published online by Cambridge University Press

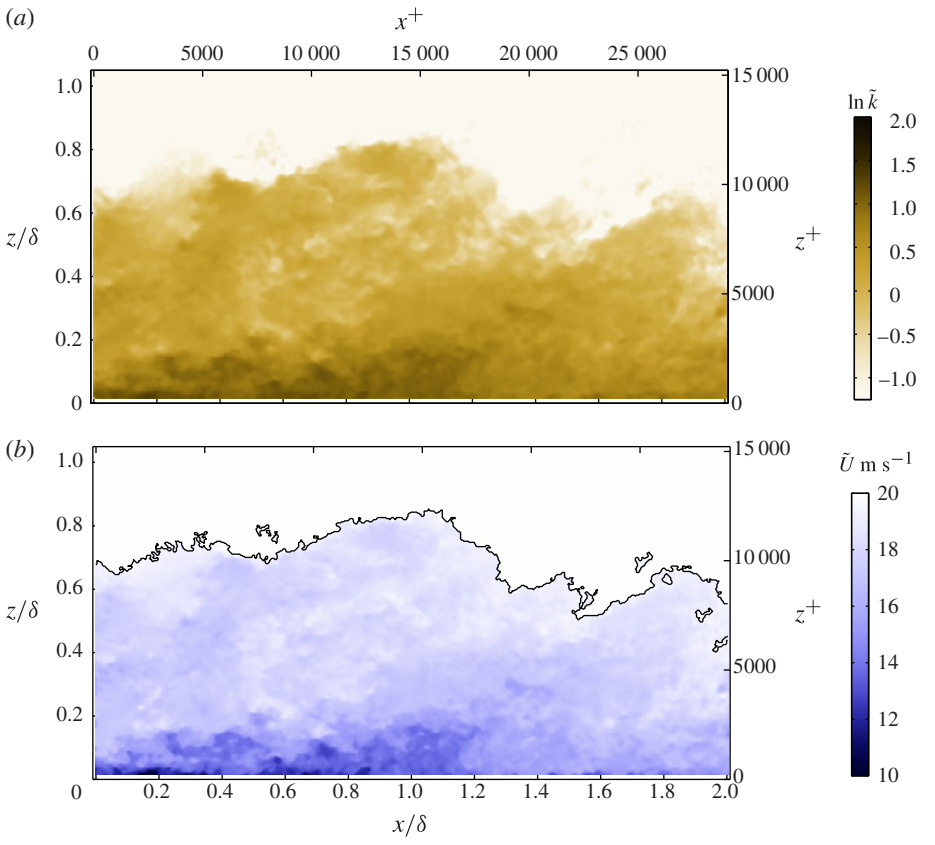


FIGURE 2. (Colour online) Example of an interface. (*a*) Contours of $\ln \tilde{k}$. (*b*) ——, outline of the interface obtained from a contour algorithm over $\tilde{k}$ in (*a*). Contours are shown for the total streamwise velocity $\tilde{U}$.

Previous intermittency measurements in boundary layers have established that the probability distribution of the instantaneous interface location z_{i} has a Gaussian shape while its cumulative distribution results in an error function that is equivalent to the intermittency profile. The following steps are taken to determine the appropriate threshold for $\tilde{k}$.

(*a*) A threshold value k_{th} is selected that corresponds to the known free-stream turbulence intensity. It is noted that this will be specific to each experimental facility.

(*b*) A binary representation of the flow is obtained for all vector fields (here 1250) using this threshold. Regions with $\tilde{k} < k_{th}$ are considered non-turbulent and assigned a value of 1 while regions where $\tilde{k} \geqslant k_{th}$ are considered as turbulent and assigned a value of 0.

(*c*) Ensemble average of the binary representation across the images and in the streamwise direction gives the intermittency profile.

(*d*) In each frame, a contour algorithm on the binary representation is used to generate contour lines at a level of 0.5. The resulting contour line demarcates

https://doi.org/10.1017/jfm.2013.641 Published online by Cambridge University Press

the turbulent and non-turbulent regions. The coordinate set $I = [x_i, z_i]$ of the contour line is the interface.

(*e*) The local interface positions from all vector fields are determined and employed to obtain its mean (Z_i) and standard deviation (σ_i).

(*f*) Various values of the kinetic energy thresholds are checked in increments of 0.01 such that the following two conditions are satisfied: (i) the resulting intermittency profile from step (*c*) agrees with an error function; and (ii) the mean and standard deviation of z_i from step (*e*) are such that $Z_i + 3\sigma_i \approx \delta$. This ensures that the intermittency beyond $z = \delta$ is essentially zero and consistent with the definition of the boundary-layer thickness.

From the above procedure a threshold of $k_{th} = 0.12$ is determined for the present data. It is re-emphasized that the chosen threshold value depends on the free-stream turbulence intensity of the wind tunnel as well as any noise in the PIV measurements. The present threshold of 0.12 is found to produce a good agreement between the intermittency profile from the PIV data and those from hotwire data (see § 4). The results pertaining to the small- and large-scale characteristics of entrainment in § 7 are qualitatively robust to this threshold value. An example of an interface determined by this approach is plotted in figure 2(*b*) over contours of instantaneous streamwise velocity field.

The instantaneous interface is clearly not smooth. The actual boundary-layer interface is a two-dimensional surface, however with planar PIV we can only capture a two-dimensional vector field and thereby the interface here is a line in the streamwise/wall-normal plane. We shall often refer to this as the interface outline. In the example shown, the interface outline resides well below the boundary-layer thickness δ, and this is the typical case as δ is the limit beyond which turbulent fluctuations cease to exist. It is seen that instantaneously the interface location relative to the wall varies significantly over the streamwise distance of 2δ. Large-scale indentations are present in the outline giving rise to the appearance of bulges and valleys. The interface location is also not monotonic in x, i.e. the interface folds back onto itself and hence at a particular streamwise location multiple TNTIs could be present. Large-scale indentations are present along with smaller pockets and further detailed examination shows that the outline is seemingly 'wrinkled' at even smaller scales. In many vector fields, 'pockets' of non-turbulent fluid are identified below the interface, surrounded completely by turbulent fluid. Similar pockets of turbulent fluid are also seen in the potential flow region. These pockets are probably three-dimensional fluid zones that are engulfed and in the process of becoming part of the turbulent flow due to the presence of vorticity at its boundary. In this paper we will solely focus on the entrainment that occurs on the interface that extends from the left edge to the right edge of the vector field.

4. Geometrical properties of the interface

In this section we examine the characteristics of the interface primarily for its geometrical aspects. The probability density function (p.d.f.) for the instantaneous interface height z_i is plotted in figure 3(*a*). The p.d.f. of z_i is obtained after combining the coordinate set $I = [x_i, z_i]$ from all vector fields. The p.d.f. exhibits a normal distribution with a mean interface location $Z_i = 0.67\delta$ and standard deviation $\sigma_i = 0.11\delta$. The mean interface location and its width agrees well the previous experiments listed in table 1. (Note that earlier studies adopted δ_{99} or $\delta_{99.5}$ as the definition of the boundary-layer thickness which are smaller than δ used in this paper

https://doi.org/10.1017/jfm.2013.641 Published online by Cambridge University Press

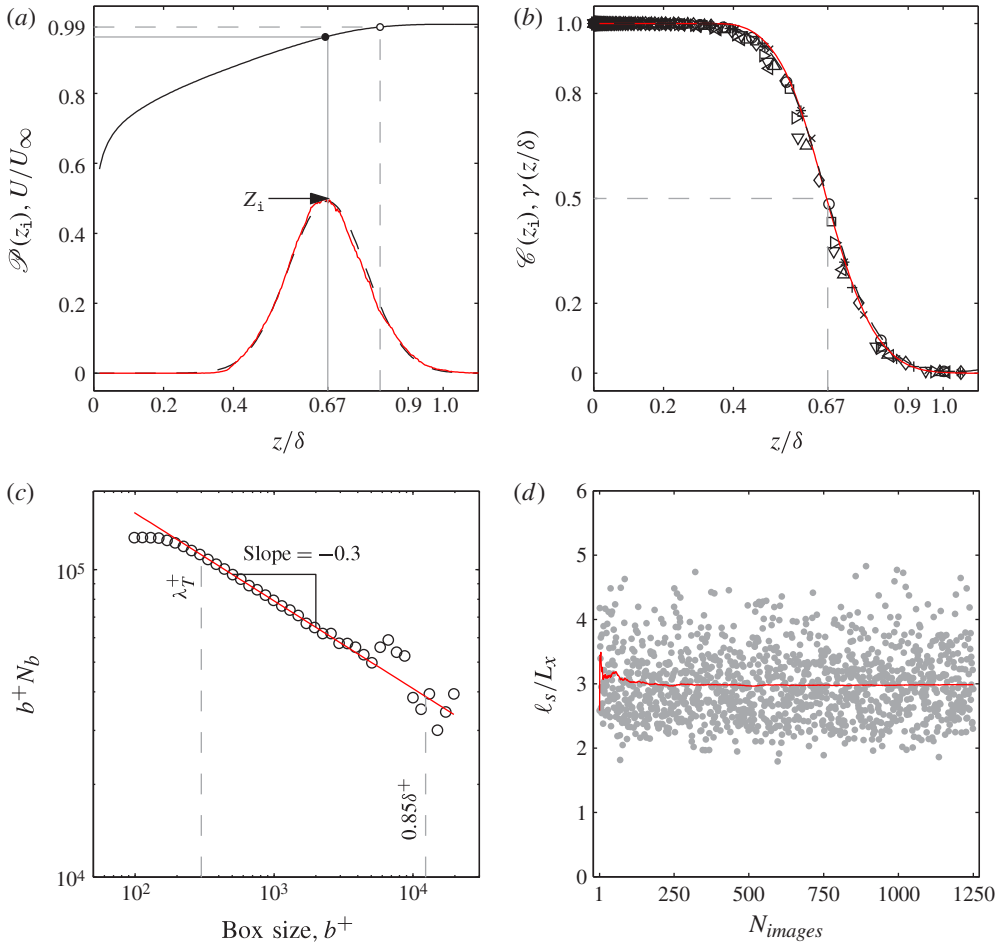


FIGURE 3. (Colour online) Properties of the interface. (*a*) —— (shown in red online), p.d.f. $\mathscr{P}$ of z_i; – – – (shown in blue online), normal distribution with mean equal to 0.67 and standard deviation as 0.11; —— (shown in black), U/U_∞. (*b*) Intermittency γ: symbols, γ from hotwire data of Kulandaivelu (2012); —— (shown in red online), cumulative distribution $\mathscr{C}$ of z_i; – – – (shown in blue online), γ from streamwise averaging of turbulent/non-turbulent regions of PIV data. (*c*) ○, number of boxes versus box size in inner units; —— (shown in red online), least-squares fit to $\ln b^+N_b$ versus $\ln b^+$. (*d*) Gray •, length of the interface outline over a unit streamwise length; —— (shown in red online), cumulative average of $\ell_s/L_x \to 3$ for 1250 vector fields.

for a particular Reynolds number.) A normal distribution fitted to the data provides a very good model for the p.d.f. of z_i except for deviation near the tail on either side of the mean (which is evident on a logarithmic vertical axis). It is noted that the interface resides mostly below $z = \delta$ (as seen in figure 2). This is obvious from the fact that the boundary-layer thickness δ is the outermost boundary of the turbulent region beyond which fully non-turbulent flow exists. If the instantaneous interface reaches above δ it would imply that the turbulent region has extended beyond δ and such a scenario is inconsistent with a proper definition of δ. The interface identified in the current study using criteria of (3.1) rarely reaches beyond $z = \delta$ which is

https://doi.org/10.1017/jfm.2013.641 Published online by Cambridge University Press

	$Re_\tau = \delta u_\tau/\nu$	Z_i/δ	σ_i/δ	σ_i/Z_i
Corrsin & Kistler (1955)	<2000	0.80	0.16	0.20
Kovasznay *et al.* (1970)	1240	0.78	0.14	0.18
Hedley & Keffer (1974*a*)	5100	0.75	0.24	0.32
Chen & Blackwelder (1978)	1190	0.82	0.13	0.16
Semin *et al.* (2011)	600	0.60	0.09	0.15
Present study (hotwire)	2700–22 000	0.64–0.67	0.11–0.13	0.16–0.2
Present study (PIV data)	14 500	0.67	0.11	0.167

TABLE 1. Comparison of mean position and width of the TNTI. The hotwire data analysed in the present study is from Kulandaivelu (2012). The value of δ is as reported in the respective studies.

obvious from the diminishing tail of the p.d.f. in figure 3(*a*). The mean velocity of the boundary layer is also plotted on the ordinate in figure 3(*a*). At the mean interface location ($Z_i/\delta \approx 0.67$) we find $U/U_\infty = 0.96$. The wall-normal location $z = \delta_{99}$ at which $U/U_\infty = 0.99$ occurs is also indicated for reference. A significant proportion of the boundary-layer interface extends beyond δ_{99}.

It is also known that the cumulative distribution function of z_i is equivalent to the mean intermittency at the edge of the layer (Corrsin & Kistler 1955). The cumulative distribution $\mathscr{C}(z_i)$ is plotted in figure 3(*b*) as a solid (red) line. Also shown in the figure is the intermittency γ calculated directly from the vector fields by streamwise averaging of the turbulent and non-turbulent zones which are identified using the procedure in § 3 using dashed (blue) line. Intermittency estimated from both approaches is in very good agreement with each other. For comparison with high Reynolds number data over a range of Reynolds number the intermittency is also determined from hotwire data of Kulandaivelu (2012) for a range of $Re_\tau = 2700$–$22\,000$ and plotted in figure 3(*b*) using symbols. The intermittency for the hotwire measurements is calculated by applying a threshold of 0.05 on a detector function defined equal to $100 \times (1 - \tilde{U}/U_\infty)^2$. The detector function for hotwire is analogous to (3.1) used for the PIV data. The regions in the $\tilde{U}$-signal over which $100 \times (1 - \tilde{U}/U_\infty)^2$ is greater than 0.05 are considered turbulent and the rest as the non-turbulent. For the PIV data a higher threshold is adopted due to the noise in the velocity estimates in the outer part. We find that intermittency profiles from hotwire and PIV measurements are in excellent agreement. Furthermore, it can be seen that the intermittency profiles collapse for a wide range of Reynolds numbers, which indicates universality. Since the cumulative distribution of z_i is equivalent to the intermittency γ, we can conclusively say that statistical properties of z_i also have a universal behaviour. Therefore, the mean interface location Z_i and its standard deviation σ_i normalized by the local boundary-layer thickness δ are Reynolds number independent. These intermittency characteristics are different from the universal behaviour in a rough-wall boundary layer (Antonia 1972) and in a boundary layer with streamwise pressure gradient (Fiedler & Head 1966).

It is obvious from the spread of p.d.f. of z_i that the instantaneous location of the interface reaches as deep as $z/\delta = 0.4$ and up to the boundary-layer edge. The large-scale indentations that appear as bulges and valleys are present along with small-scale contortions that appear like wrinkles on the interface outline (figure 2). Such fragmented and convoluted features motivate us to examine the interface outline

https://doi.org/10.1017/jfm.2013.641 Published online by Cambridge University Press

for fractal characteristics. The notion that the TNTI adheres to fractal geometry was first demonstrated experimentally by Sreenivasan & Meneveau (1986). Recently de Silva *et al.* (2013) demonstrated that the fractal dimension of the TNTI in a turbulent boundary layer at high Reynolds numbers is between 2.3 and 2.4. They utilized the kinetic energy criteria to determine the TNTI for two different Reynolds numbers and found that the fractal characteristics are robust to the chosen kinetic energy threshold. Here we briefly discuss the fractal nature of the TNTI to motivate the exposition of multiscale entrainment phenomena that is discussed in § 7. The fractal dimension of the interface is calculated using the box-counting method described by Prasad & Sreenivasan (1989) and is only briefly discussed here. The field of view is divided into square boxes of a certain size (box size, b^+) and we count the number of boxes (N_b) within which the interface is present. Each box size can be considered as a measuring unit. The procedure is repeated for different box sizes over the 1250 interface outlines considered in our analysis. The resulting average variation of N_b versus b^+ appears linear on a log–log plot. However, deviations from the linear slope are hard to observe in the log–log plot of N_b versus b^+. Therefore, we multiply N_b with b^+ to plot b^+N_b versus b^+ in figure 3(*c*). It is intuitive that as the size of box decreases the number of boxes required to measure the interface of a particular length increases. The linear trend of $\ln(b^+N_b)$ versus $\ln b^+$ implies that $N_b \propto (b^+)^{-D_f+1}$. The slope is determined by fitting within the bounds $\lambda_T^+ < b^+ < 0.2\delta^+$. The slope of the linear trend in figure 3(*c*) is approximately -0.3 which results in the fractal dimension being $D_f \approx 2.3$. This value of the fractal dimension of the interface, within experimental error, is in good agreement with the values obtained in previous studies where the interface was identified using different approaches (Sreenivasan *et al.* 1989; Meneveau & Sreenivasan 1990). In figure 3(*c*) we have also shown two vertical lines at $\lambda_T^+ \approx 300$ and $0.85\delta^+$. These represent the small- and large-scale estimates of entraining motions derived in § 7 and will be discussed therein. It is noted in figure 3(*c*) that approximately below the Taylor microscale the scales of the interface deviate from the fractal characteristic. On the other hand, at the outer limit of figure 3(*c*) the data fails to show a clear fractal behaviour. This is a limitation suffered in obtaining converged statistics corresponding to large scales. The largest box size used in calculating N_b corresponds to 400 vectors and is equivalent to 1.36δ. For a box size in this range the box count is saturated at two as only two boxes would be required to occupy the interface over a domain of $2\delta \times 1.1\delta$. One would need an even larger field of view than the current experiment to obtain the converged fractal behaviour at box size of $O(\delta)$.

In the present experimental set-up we have a field of view that is 2δ long in the streamwise direction. It is obvious from figure 2 and the fractal characteristic of the interface that the length of the interface measured along on the path $I = [x_i, z_i]$ will be greater than the streamwise distance L_x ($=2\delta$). The length of interface ℓ_s is calculated in all PIV vector fields and normalized by the streamwise distance L_x and are shown in figure 3(*d*). The interface length is at least twice the streamwise distance and is often as high as $5L_x$. This figure quantifies the contorted feature of the interface outline. Both large-scale bulges/valleys and small-scale wrinkles contribute to the increased length. The moving average of interface length per unit streamwise distance from all 1250 vector fields quickly converges to 3.0, indicated by the solid (shown in red online) line in figure 3(*d*). In theory, if we had access to similar measurements in the spanwise/wall-normal plane and the interface outline was determined on this plane, then the fractal dimension of the interface would also equal 2.3 (see § 2.2 in

https://doi.org/10.1017/jfm.2013.641 Published online by Cambridge University Press

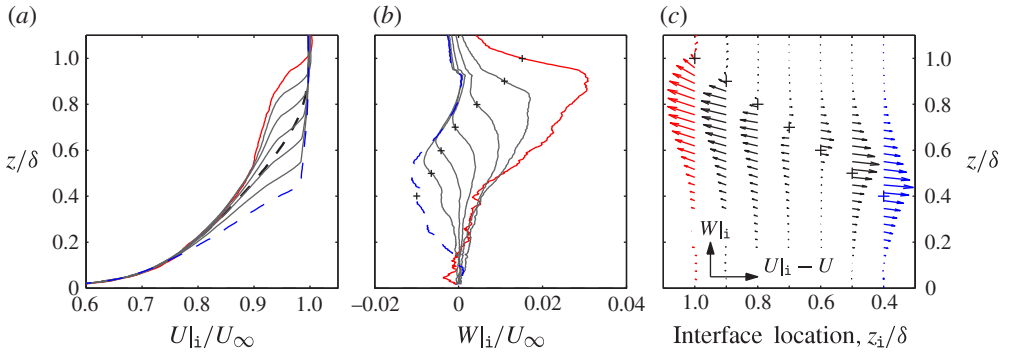


FIGURE 4. (Colour online) Conditionally averaged profiles of (*a*) $U|_i$ and (*b*) $W|_i$ for different z_i/δ. —— (shown in red online), average profile when $0.95 < z_i/\delta \leqslant 1.05$; subsequent (grey) profiles are for $0.85 < z_i/\delta \leqslant 0.95$, $0.75 < z_i/\delta \leqslant 0.85$ and so on up to $0.35 < z_i/\delta \leqslant 0.45$ which is shown as – – – (shown in blue online). Mean U/U_∞ is plotted in (*a*) as a dashed black line. (*c*) Conditional vector field (relative to the mean) in a wall-normal line when the interface is at a particular reference height. '+' signs in (*b*) and (*c*) indicates the reference wall-normal height for conditional averages.

Sreenivasan 1991). In that case the interface length in the spanwise direction would also be on average three times than the unit spanwise distance (Paizis & Schwarz (1974) have shown this for a turbulent wall jet). Therefore, the two-dimensional instantaneous TNTI can be expected to be nine times larger in area compared with the unit area it resides on. The increased surface area would amplify the aggregate entrainment by small-scale nibbling. These properties pose the following questions. What is the size of small-scale nibbling? What is the role played by the large-scale bulges/valleys in the net entrainment mechanism? We will partially address these questions in § 7.

5. Dynamics at the interface

Figure 4(*a*) and (*b*) show profiles of conditionally averaged streamwise and wall-normal velocities, respectively. To find the conditional average we first determine the interface with the procedure described in § 3. The interface at a particular streamwise location can be multivalued, i.e. as one approaches the free stream from the wall, multiple turbulent/non-turbulent boundaries would be encountered because the interface folds back onto itself. The 'lower envelope' of the interface is considered, which guarantees that the flow below is fully turbulent. The lower envelope is the coordinate set of points representing the projection of the wall on to the interface. Thereafter, for a particular wall-normal location of interest where the interface is found, instantaneous velocity profiles from all vector fields are collected and averaged. The conditionally averaged profile of streamwise velocity when the interface is at a particular z_i location is denoted as $U|_i$. For example, the average of instantaneous profiles where the lower envelope of the interface is between $0.95 < z_i/\delta \leqslant 1.05$ is shown by the solid (shown in red online) line in figure 4(*a*), while the profile for $0.35 < z_i/\delta \leqslant 0.45$ is the dashed (shown in blue online) line.

It is obvious that away from the wall the conditionally averaged profiles are significantly different in characteristics from the mean U/U_∞ (shown by the dashed

https://doi.org/10.1017/jfm.2013.641 Published online by Cambridge University Press

black line). For $0.95 < z_{\mathrm{i}}/\delta \leqslant 1.05$ a step change in $U|_{\mathrm{i}}$ appears near $z/\delta \approx 0.9$. A steep change in velocity is present in all conditional profiles where $U|_{\mathrm{i}}$ typically increases above $0.94U_\infty$. Each profile has a very sharp change in wall-normal gradient near the location of the interface. The gradient near the wall is comparable with the local mean shear, while at further height beyond the interface location for which the profiles are conditionally averaged, the gradient is nominally zero. For $0.35 < z_{\mathrm{i}}/\delta \leqslant 0.45$ the averaged velocity beyond the interface is less than U_∞ throughout. Figure 4(*b*) plots the conditionally averaged wall-normal velocity $W|_{\mathrm{i}}$ and complements figure 4(*a*). For $0.95 < z_{\mathrm{i}}/\delta \leqslant 1.05$ a bulk positive $W|_{\mathrm{i}}$ is seen above $z/\delta \approx 0.5$. A positive $W|_{\mathrm{i}}$ agrees with the notion that upwards velocity is associated with the interface being 'lifted' away from its mean location Z_{i}/δ. (Note that the interface is neither a material property nor a dynamical characteristic of the flow. It represents the boundary between the turbulent/non-turbulent regions. Hence, when we say that the interface is moving we here imply that the turbulent and non-turbulent regions along with its boundary are convected together.) On the other hand for $0.35 < z_{\mathrm{i}}/\delta \leqslant 0.45$ a bulk negative $W|_{\mathrm{i}}$ exists below $z/\delta \approx 0.9$, which again correlates well with the interface being 'pushed' towards the wall, an observation also made by Jiménez *et al.* (2010). Note that $W|_{\mathrm{i}}$ is positive or negative for a significant wall-normal distance above the reference interface location ('+' sign in the figure). These characteristics are readily observed when the conditional vector field (relative to the mean) in a wall-normal line is examined in figure 4(*c*). Here the streamwise component of the vectors is relative to the mean velocity, i.e. $U|_{\mathrm{i}} - U$. Each column of vectors in figure 4(*c*) corresponds to the conditional wall-normal averages in figure 4(*a*) and (*b*) when the interface is a particular z_{i}/δ ('+' sign in the figure). The resultant vectors show that the flow relative to the mean velocity is significantly altered not only below the interface but also above it with varying interface heights. This implies that the potential streamlines are inclined differently compared with the mean flow. The mechanisms that are responsible for the interface to be at different heights with a correspondingly imposed bulk wall-normal velocity either originate from the boundary layer as there are no external perturbations in the free stream (Kovasznay *et al.* 1970) or result from a large-scale instability at the interface (Townsend 1966).

So far we have looked at the bulk velocities above and below the interface for its different positions relative to the wall. From figure 4 it is concluded that a significant change in streamwise momentum occurs over a small wall-normal distance within which the interface lies. We shall now examine the conditional statistics in the close vicinity of the interface in figure 5. A moving frame is considered here that is parallel to the Cartesian frame, while the origin of this frame is on the interface irrespective of where the interface is located. As one moves along the interface, profiles for instantaneous $\tilde{U}$, $\tilde{W}$ and $\tilde{\Omega}_y$ are collected over the ordinate z–z_{i} (the non-turbulent pockets and the turbulent islands, e.g. as seen in figure 2, are excluded from the statistics). These profiles now have the instantaneous z_{i} as the wall-normal reference and the subsequent averaging of any statistics will be denoted by angled brackets $\langle\ \rangle$ hereafter. The resulting mean streamwise velocity $\langle\tilde{U}\rangle$ and wall-normal velocity $\langle\tilde{W}\rangle$ are plotted in figure 5(*a*) and (*b*), respectively. The ensemble averages $\langle\tilde{U}\rangle$ and $\langle\tilde{W}\rangle$ are equivalent to the averages of profiles in figure 4(*a*) and (*b*), respectively, with weighting proportional to the probability distribution of z_{i}.

A distinct rise in $\langle\tilde{U}\rangle$ is observed in figure 5(*a*) as one crosses the interface from the turbulent region to the non-turbulent region. The steep rise in $\langle\tilde{U}\rangle$ is consistent

https://doi.org/10.1017/jfm.2013.641 Published online by Cambridge University Press

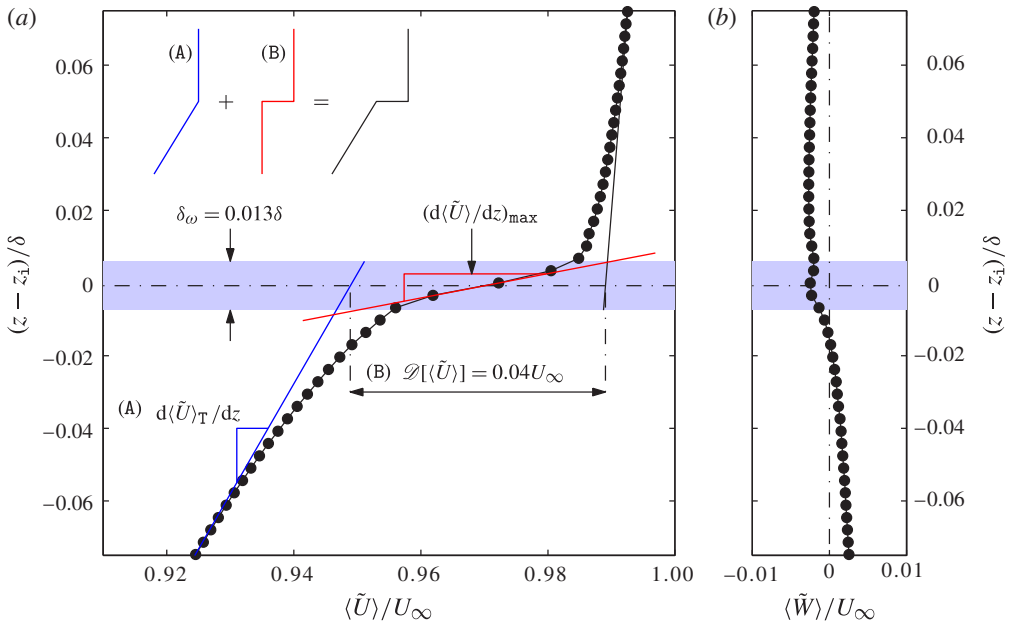


FIGURE 5. (Colour online) Conditionally averaged statistics with respect to the interface z_{i}. (*a*) —●—, $\langle\tilde{U}\rangle/U_\infty$; solid lines indicate local slopes. (*b*) —●—, $\langle\tilde{W}\rangle/U_\infty$. The shaded region in each figure represents the region equivalent to the vorticity thickness δ_ω and is indicative of the superlayer.

with the step-like increase observed for $U|_{\mathrm{i}}$ profiles in figure 4(*a*) and the existence of a superlayer at the TNTI (Corrsin & Kistler 1955). We note as an aside that, since Corrsin & Kistler (1955) first proposed the existence of a *superlayer*, the majority of studies that followed interchangeably used the terms interface and superlayer. According to Corrsin & Kistler (1955), vorticity is imparted to the non-turbulent flow by viscous diffusion. Thereafter the vorticity gets further amplified by the action of pre-existing vorticity in the turbulent region and the local shear. Experimentally, it has been not possible to distinguish between these two mechanisms due to measurement limitations. However, recently da Silva & Taveira (2010) and da Silva & dos Reis (2011) have utilized high-resolution direct numerical simulation to identify a region where viscosity effects are prominent (called the 'viscous superlayer') and a region where a peak in vorticity occurs (called the interface). As in our study such a distinction is not possible we will adopt the conventional terminology and refer to the region where the peak in vorticity occurs (in figure 6*a*) and that coincides with the region where a jump is observed in figure 5(*a*) as the superlayer.

The increase in $\langle\tilde{U}\rangle$ across the interface, denoted as $\mathscr{D}[\langle\tilde{U}\rangle]$ is approximately 4 % of the free-stream velocity U_∞. The profile of $\langle\tilde{U}\rangle$ in the turbulent and non-turbulent zone is linear but with different gradients (Kovasznay *et al.* 1970). The gradient in the turbulent part is indicated as $\mathrm{d}\langle\tilde{U}\rangle_{\mathrm{T}}/\mathrm{d}z$. The adjustment of gradient (from high in the turbulent part to near zero in the non-turbulent part) occurs in a narrow region over which the local gradient reaches a maximum, indicated as $\mathrm{d}\langle\tilde{U}\rangle/\mathrm{d}z|_{\max}$ in figure 5(*a*). One can then define a vorticity thickness (e.g. Brown & Roshko 1974) based on the

https://doi.org/10.1017/jfm.2013.641 Published online by Cambridge University Press

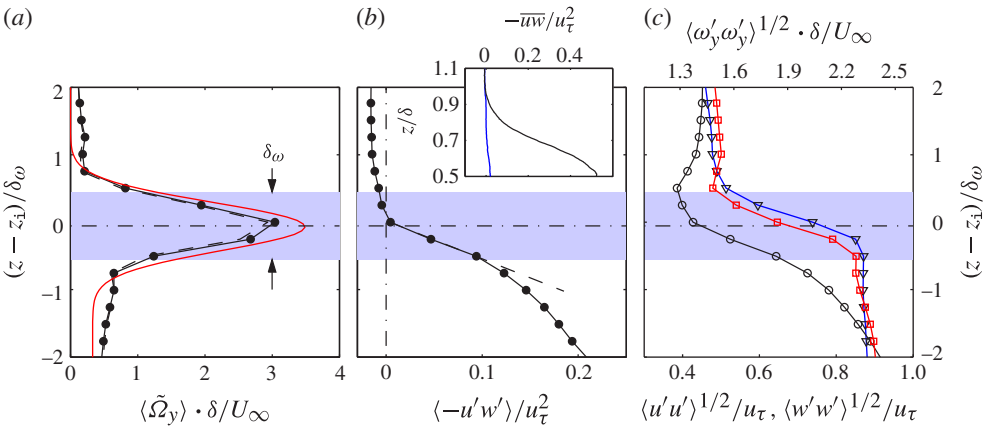


FIGURE 6. (Colour online) Conditionally averaged statistics with respect to the interface z_i. (*a*) —●—, spanwise vorticity $\langle\tilde{\Omega}_y\rangle\cdot\delta/u_\tau$; solid (shown in red online) line, (5.5); dashed (black) line, $\mathrm{d}\langle\tilde{U}\rangle/\mathrm{d}z$. (*b*) —●—, Reynolds shear stress $\langle -u'w'\rangle/u_\tau^2$; dashed line is the locally linear behaviour. Insert on (*b*): solid (shown in blue online) line, Reynolds shear stress in the identified non-turbulent zones only; solid (black) line, Reynolds shear stress $-\overline{uw}$. (*c*) —▽— (shown in blue online), r.m.s. of the spanwise vorticity $\langle\omega_y'\omega_y'\rangle^{1/2}$ (top abscissa); —○— (black), r.m.s. of the streamwise fluctuations $\langle u'u'\rangle^{1/2}$; —□— (shown in red online), r.m.s. of wall-normal fluctuations $\langle w'w'\rangle^{1/2}$ (bottom abscissa). The shaded region in each figure represents the region equivalent to the vorticity thickness δ_ω and is indicative of the superlayer.

measured change in $\langle\tilde{U}\rangle$ and its local gradient as

$$\delta_\omega \equiv \frac{\mathscr{D}[\langle\tilde{U}\rangle]}{\left.\dfrac{\mathrm{d}\langle\tilde{U}\rangle}{\mathrm{d}z}\right|_{\max}}. \tag{5.1}$$

In the present study we find that $\delta_\omega = 0.013\delta$ or $\delta_\omega^+ = 195$ for our Reynolds number and δ_ω is shown as the shaded region in figure 5. In our study the finite interrogation window size is likely to have a filtering effect on the resolved velocity gradient across the superlayer and the subsequent estimate of δ_ω. The experimental value of δ_ω is thus considered as an upper bound for the superlayer thickness at this particular Reynolds number.

It is seen that the most significant change in $\langle\tilde{U}\rangle$ occurs over the region equivalent to the vorticity thickness and hence δ_ω is considered as the superlayer width. A similar steep rise in streamwise momentum has been previously observed by Hedley & Keffer (1974*a*) who found a sharp increase in derivatives of velocity components across the TNTI using conditional sampling. Chen & Blackwelder (1978) used temperature as a passive contaminant to show that steep variation in velocities in the outer part are associated with temperature fronts that essentially are 'backs' of the turbulent bulges. More recently, Semin *et al.* (2011) used tomographic PIV data to document the conditionally averaged profiles of streamwise momentum and spanwise vorticity similar to those in figure 5. Their results do not quantitatively agree with our experiments, and this is attributed to the low Reynolds number in their study ($Re_\tau = 600$). The sudden change in streamwise momentum is often referred to as a

https://doi.org/10.1017/jfm.2013.641 Published online by Cambridge University Press

'jump' in velocity across the interface and has been found in TNTI of wakes and jets (Bisset *et al.* 2002; Westerweel *et al.* 2005).

The conditional profile of $\langle \tilde{W} \rangle$ lacks a similar distinct jump across the interface. It is known that across the interface a jump in the tangential velocity component occurs (e.g. Bisset *et al.* 2002; Holzner *et al.* 2007; Westerweel *et al.* 2009), while the velocity component normal to the local interface is uniform (Reynolds 1972). The turbulent boundary layer under zero pressure gradient grows gradually ($\mathrm{d}\delta/\mathrm{d}x \approx 0.012$ at $Re_\tau = 14\,500$, see appendix A) and the growth rate decreases further downstream. Although the instantaneous interface is contorted the average interface is bounded by the slow growth rate of the boundary layer itself, i.e. $\mathrm{d}Z_{\mathrm{i}}/\mathrm{d}x \approx (Z_{\mathrm{i}}/\delta) \cdot (\mathrm{d}\delta/\mathrm{d}x)$ ($Z_{\mathrm{i}}/\delta \rightarrow$ constant, see § 4). Under such conditions the wall-normal velocity $\tilde{W}$ will contribute the most to the mean velocity normal to the mean interface while the streamwise velocity $\tilde{U}$ will dominate the mean tangential velocity. The presence of a jump in the $\langle \tilde{U} \rangle$ profile and the relative absence of a jump in $\langle \tilde{W} \rangle$ profile is thereby consistent. We find from figure 5(*b*) that the normal velocity at the interface $\langle \tilde{W}_{\mathrm{i}} \rangle = -0.05$ m s^{-1} is negative and consistent with the understanding that momentum from the non-turbulent region is being brought into the turbulent region by entrainment. We can proceed further by making the approximation that the velocity components in a frame of reference on the interface and parallel to the coordinates x and z are sufficient to study the average statistics about the interface in lieu of components that are locally tangential and normal to the outline s.

For further observations of the conditional statistics at the interface we normalize the wall-normal distance relative to the local interface (z–z_{i}) by the vorticity thickness δ_ω in figure 6. The observed jump in streamwise velocity is accompanied by a corresponding peak in spanwise vorticity in figure 6(*a*). The theoretical analysis of Reynolds (1972) predicts a discontinuity in mean vorticity across the interface. The peak in spanwise vorticity resides within the region indicated by the vorticity thickness δ_ω. The spanwise vorticity is finite and approximately constant in the turbulent region and this observation is consistent with the linear slope of $\langle \tilde{U} \rangle$ on the turbulent side in figure 5(*a*). The vorticity magnitude approaches near zero on the non-turbulent side. As one moves along the interface, homogeneity can be assumed in the tangential direction due to the slow growth of mean interface location, i.e. $\partial(\ )/\partial x \rightarrow 0$ for mean quantities, and the same can be assumed for the conditional averages. Therefore, the mean vorticity within the interface in figure 6(*a*) can be expressed as

$$\langle \tilde{\Omega}_y \rangle \approx \frac{\mathrm{d}\langle \tilde{U} \rangle}{\mathrm{d}z}. \tag{5.2}$$

This assumption is easily verified by the fact that the wall-normal gradient of streamwise velocity in figure 5(*a*) alone is sufficient to account for the mean vorticity within the interface in figure 6(*a*) (see the dashed line in figure 6*a*). The behaviour of velocity (and thereby the vorticity) across the TNTI can be modelled as the superposition of two components (Bisset *et al.* 2002; Westerweel *et al.* 2005): (A) a profile with linear slope in the turbulent region and zero slope in the non-turbulent region and (B) a step change in velocity (from being non-zero in the turbulent flow to zero in the non-turbulent flow) in the form of a Heaviside step function $\boldsymbol{H}(\xi)$. This simplified model is depicted in figure 5(*a*) and can be written as

$$\langle \tilde{U} \rangle(\xi) = U_\infty + \underbrace{\frac{\mathrm{d}\langle \tilde{U} \rangle_{\mathrm{T}}}{\mathrm{d}\xi} \cdot \xi\,[1 - \boldsymbol{H}(\xi)]}_{\text{(A)}} - \underbrace{\mathscr{D}[\langle \tilde{U} \rangle]\,[1 - \boldsymbol{H}(\xi)]}_{\text{(B)}}. \tag{5.3}$$

https://doi.org/10.1017/jfm.2013.641 Published online by Cambridge University Press

Here we adopt $\xi = z - z_{\mathrm{i}}$ for convenience. The above equation can be differentiated with respect to ξ to obtain

$$\frac{\mathrm{d}\langle\tilde{U}\rangle}{\mathrm{d}\xi} = \mathscr{D}[\langle\tilde{U}\rangle]\,\delta(\xi) + \frac{\mathrm{d}\langle\tilde{U}\rangle_{\mathrm{T}}}{\mathrm{d}\xi}\,[1 - \boldsymbol{H}(\xi)]. \tag{5.4}$$

Even though mathematically the jump in $\langle\tilde{U}\rangle$ is represented across an infinitely small region, in reality the viscous effects play a role and the jump occurs over a small but finite region. Also, in the experimental data there exists a random error in locating the interface over its finite width for discretely spaced data (it is recalled that in the present study the distance between adjacent vectors is 50 viscous units). The conditional averages would suffer from this uncertainty and therefore (5.4) is convolved with a Gaussian kernel ($\exp[-\xi^2/2/R^2]$) to account for the 'smearing' of statistics:

$$\langle\tilde{\Omega}_y\rangle \approx \frac{\mathrm{d}\langle\tilde{U}\rangle}{\mathrm{d}\xi} = \mathscr{D}[\langle\tilde{U}\rangle]\frac{1}{\sqrt{2\pi}\,R}\exp\left(-\frac{\xi^2}{2R^2}\right) + \frac{\mathrm{d}\langle\tilde{U}\rangle_{\mathrm{T}}}{\mathrm{d}\xi}\left[\frac{1}{2} - \frac{1}{2}\mathrm{erf}\left(\frac{\xi}{\sqrt{2}R}\right)\right]. \tag{5.5}$$

Here 'erf' is the error function. Equation (5.5) is in reasonably good agreement with the measured $\langle\tilde{\Omega}_y\rangle$ with the parameter $Ru_\tau/\nu = 75$ in figure 6(*a*) (with measured $\mathscr{D}[\langle\tilde{U}\rangle]$ and $\mathrm{d}\langle\tilde{U}\rangle_{\mathrm{T}}/\mathrm{d}\xi$ from figure 5*a*). The convolution with a Gaussian kernel and the subsequent agreement with the data implies that the error in determining the interface is indeed random (a Gaussian process). One cannot deduce the size of the superlayer based on the width of such a Gaussian kernel, as it only sets an upper limit to the actual thickness.

Fluctuating components of $\tilde{U}$, $\tilde{W}$ and $\tilde{\Omega}_y$ are found with respect to the conditional mean profiles in figures 5(*a*), 5(*b*) and 6(*a*), respectively, and referenced to the z_{i} ordinate. These are denoted as u', w' and ω_y' for the streamwise, wall-normal and vorticity fluctuations, respectively. The profiles for Reynolds shear stress and the root mean square (r.m.s.) of fluctuations are plotted in figure 6(*b*) and (*c*), respectively. The conditional Reynolds shear stress at the interface is found to be zero and rapidly increases in the turbulent region. Note that the location where $\langle -u'w'\rangle$ becomes zero coincides with the peak in vorticity in figure 6(*a*). On the non-turbulent side away from the interface the Reynolds shear stress is oppositely signed and varies slowly to approach a constant value in the fully non-turbulent region. A non-zero value for the conditional Reynolds shear stress $\langle u'w'\rangle$ in the non-turbulent region immediately next to the interface is also documented by Bisset *et al.* (2002) in a wake and by Westerweel *et al.* (2009) in a jet. This behaviour should not be interpreted as the existence of non-zero eddy viscosity beyond the TNTI in a boundary layer. In the absence of vortical motions in the non-turbulent flow the eddy viscosity is zero. The finite $\langle -u'w'\rangle$ in the non-turbulent region is an artifact of the conditional averaging across the interface. As we have seen earlier, due to the changing interface heights, the potential streamlines change direction instantaneously. These bulk motions above the interface have large-scale variations in streamwise and wall-normal momentum and thus contribute to the non-zero Reynolds shear stress. As a check, we have calculated the Reynolds shear stress in the laboratory frame of reference at each wall-normal position by considering only the non-turbulent regions. Thereby the Reynolds shear stress obtained within the non-turbulent zones only is plotted versus the distance from the wall as the solid (shown in blue online) line in the inset in figure 6(*b*). The calculated Reynolds shear stress in the non-turbulent zones is indeed insignificant compared to the average Reynolds shear stress $-\overline{uw}$ in the boundary

https://doi.org/10.1017/jfm.2013.641 Published online by Cambridge University Press

layer (solid black line in the inset). Similar observations were made by Hedley & Keffer (1974*a*) and Jiménez *et al.* (2010) for boundary layers. Note that in the case of a turbulent jet/wake the width of the mean flow is defined as the half-width. This would imply that in the laboratory frame of reference a non-zero shear stress exists outside the jet/wake width, while by definition of δ in the present study no turbulence and thereby shear stress exists beyond the boundary-layer thickness.

A simplified tangential momentum balance (see equation (3.1*c*) of Reynolds 1972) relates the change in $\langle\tilde{U}\rangle$ across the superlayer to the change in the turbulent shear as

$$\mathscr{D}[\langle -u'w'\rangle] = -\langle\tilde{W}_{\mathrm{i}}\rangle\,\mathscr{D}[\langle\tilde{U}\rangle]. \tag{5.6}$$

Here $\mathscr{D}[\ ]$ is a difference operator, $\mathscr{D}[\langle -u'w'\rangle]$ and $\mathscr{D}[\langle\tilde{U}\rangle]$ are the changes in the mean Reynolds shear stress and mean tangential velocity respectively across the interface. From figure 5(*a*) and (*c*), $\mathscr{D}[\langle\tilde{U}\rangle] = 0.04U_\infty$ and $\mathscr{D}[\langle -u'w'\rangle] = -0.11u_\tau^2$, respectively. Therefore, we get

$$\langle\tilde{W}_{\mathrm{i}}\rangle = -\frac{\mathscr{D}[\langle -u'w'\rangle]}{\mathscr{D}[\langle\tilde{U}\rangle]} = -\frac{0.043}{0.80} = -0.053\ \mathrm{m\ s^{-1}}. \tag{5.7}$$

The above estimate of the normal velocity across the interface is in excellent agreement with the directly measured $\langle\tilde{W}_{\mathrm{i}}\rangle$ ($=-0.05$ m s^{-1}). The validity of condition (5.7) has also been experimentally observed by Westerweel *et al.* (2009) in turbulent jets. The quantitative agreement of (5.5) and (5.6) with the measurements indicate that we have correctly captured the TNTI dynamics and the approximations regarding the tangential and normal components of velocity are appropriate.

The r.m.s. of the fluctuating components shown in figure 6(*c*) also show a rapid increase in the r.m.s. as one crosses from the non-turbulent region to the turbulent region. The r.m.s. is non-zero above the interface which should not be interpreted as turbulence. The contribution to the r.m.s. is from the large-scale variations in the potential streamlines at the edge of the interface as the interface position moves relative to the wall. Both $\langle w'w'\rangle$ and $\langle\omega_y'\omega_y'\rangle$ profiles show antisymmetric behaviour across the interface with respect to the local magnitude at $\xi = 0$. The increase in the variance of the fluctuations is consistent with the behaviour of the mean quantities across the interface and previous observation of TNTI in jets by Westerweel *et al.* (2009).

It should be noted that (5.5) for vorticity is analogous to the vorticity in an Oseen vortex. Furthermore, in figure 5(*a*) we observe that the streamwise velocity profile resembles a shear layer, the vorticity has a Gaussian peak behaviour and the shear stress is zero at the interface and oppositely signed on either side. These characteristics indicate that a certain vortex-like feature or vortex sheet resides within the interface. If the interface is indeed populated with vortices or vortex-like motions, then the characteristic length of such motions will represent the scales at which entrainment occurs, which shall be the concern in the following sections.

6. An estimate of length scales

In this section we use two-point correlation as a tool to obtain information about dominant length scales at the boundary-layer interface. Such analysis follows from the work of Westerweel *et al.* (2005) and Ishihara, Hunt & Kaneda (2012) who calculated the spatial auto-correlation of conditional velocity along the interface. A similar approach is adopted here, although the normal velocity at the interface will be considered. In the present analysis a local kinetic energy criteria as outlined

https://doi.org/10.1017/jfm.2013.641 Published online by Cambridge University Press

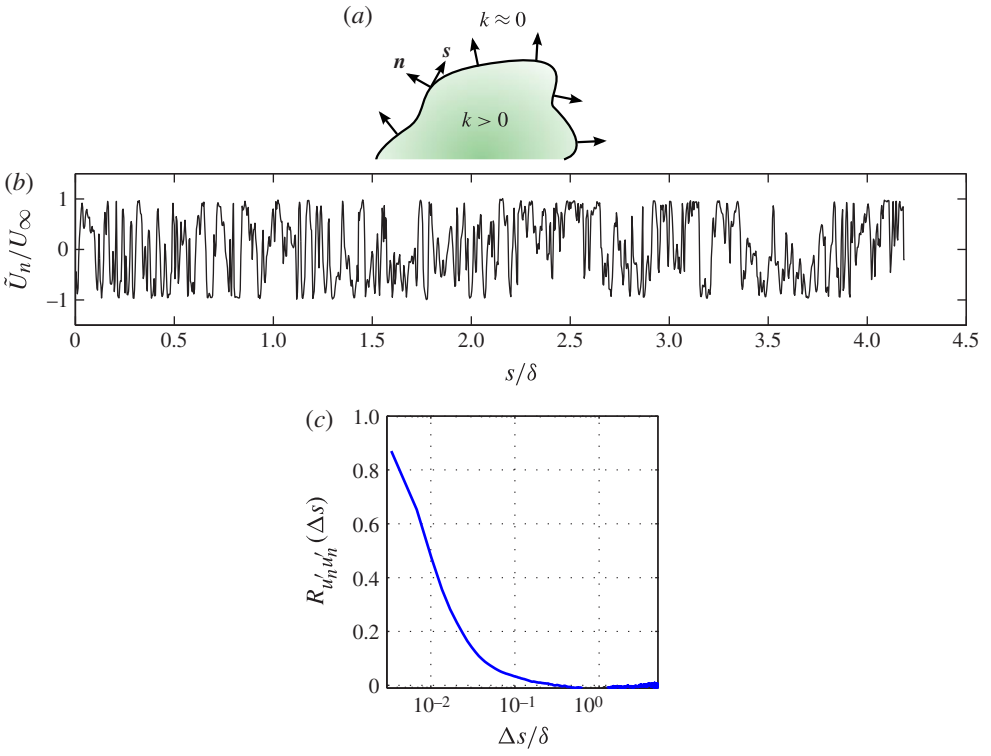


FIGURE 7. (Colour online) (*a*) Schematic for calculation of unit vector normal to the interface. (*b*) Instantaneous normal velocity at the interface of figure 2(*b*). (*c*) Auto-correlation $R_{u'_n u'_n}$ of fluctuations at the interface that are relative to the mean of $\tilde{U}_n$.

by (3.1) is applied to distinguish the turbulent from the non-turbulent region. The turbulent kinetic energy (k) is a scalar quantity. As illustrated in figure 7(*a*), within the turbulent region $k > 0$, while in the non-turbulent region $k \approx 0$. The local gradient of kinetic energy ($\partial k/\partial n$) at the interface will be normal to the instantaneous interface outline. The unit vector $\boldsymbol{n}$ that is normal to the interface is then calculated as

$$\boldsymbol{n} = -\frac{\nabla k}{|\nabla k|} \quad \text{where } \nabla = \frac{\partial}{\partial x}\hat{\boldsymbol{e}}_x + \frac{\partial}{\partial z}\hat{\boldsymbol{e}}_z. \tag{6.1}$$

Thereafter the instantaneous normal velocity ($\tilde{U}_n$) at the interface is calculated using the measured streamwise velocity $\tilde{U}_{\mathrm{i}}$ and wall-normal velocity $\tilde{W}_{\mathrm{i}}$ at the interface as

$$\tilde{U}_n = \tilde{\boldsymbol{U}}_{\mathrm{i}} \cdot \boldsymbol{n} = \tilde{U}_{\mathrm{i}} n_x + \tilde{W}_{\mathrm{i}} n_z. \tag{6.2}$$

Here, n_x and n_z are the streamwise and wall-normal components of $\boldsymbol{n}$, respectively. An example of $\tilde{U}_n$ for the interface shown in figure 2(*b*) is plotted versus the distance s along the interface in figure 7(*b*). We have considered the outward normal as positive. Since the interface is contorted and the outward normal often points in the opposite direction of the free stream, the instantaneous normal velocity fluctuates within the approximate bounds of $(-U_\infty, U_\infty)$. The sudden and rigourous change in the direction of $\tilde{U}_n$ is largely due to the change in the direction of the local normal (or tangent) of the interface, where the local tangent to the interface can be defined

https://doi.org/10.1017/jfm.2013.641 Published online by Cambridge University Press

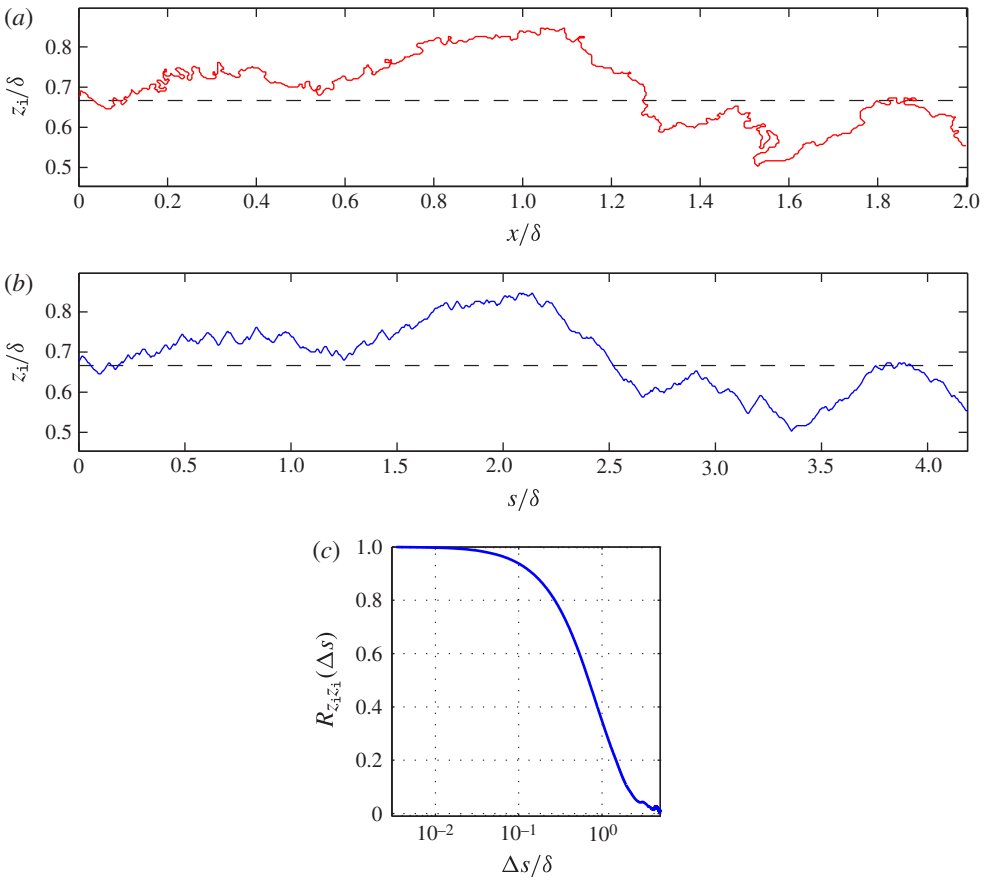


FIGURE 8. (Colour online) (*a*) Local interface height z_i as a function of the streamwise distance x. (*b*) Local interface height z_i as a function of the distance s along the interface. (*c*) Auto-correlation of $z_i(s)$.

as $\mathrm{d}z_i/\mathrm{d}s$ (see figure 8*b*). One can then think of the rapid fluctuations in $\tilde{U}_n$ a result of the small-scale contortions in the interface. If the interface lacked such small-scale features the variation of the normal velocity at the interface would be much smoother. Alternately the small-scale contortions could be characterized by examining the direction vector $\boldsymbol{n}$, however, we utilize $\tilde{U}_n$ here as it is also a relevant quantity to calculate the average mass-flux in a boundary layer at a particular Reynolds number (equation (7.12)).

The variation of normal velocity at the interface exhibits characteristics similar to a turbulent signal. It is obvious that the $\tilde{U}_n$ fluctuations have a high-frequency (small wavelength) component. To characterize the associated length scale we obtain the auto-correlation of velocity fluctuations u_n' that are normal to the interface and relative to the mean of $\tilde{U}_n$, i.e. $u_n' = \tilde{U}_n - \langle \tilde{U}_n \rangle$. The auto-correlation is calculated for all vector fields and its average is plotted in figure 7(*c*) versus the shift Δs of distance along the interface. The auto-correlation $R_{u_n' u_n'}$ shows a clear presence of small-scale features consistent with observed variation in $\tilde{U}_n$. In § 4 we have noted that the interface length is approximately three times longer than the streamwise

https://doi.org/10.1017/jfm.2013.641 Published online by Cambridge University Press

distance. Thereby, a characteristic length scale along the interface (λ_s) and the streamwise length scale (λ_x) would be also bounded by this proportionality. With that in consideration, figure 7(*c*) provides an estimate of length scale $\Lambda_x^+ \approx 290$ as the wavelength corresponding to the peak in premultiplied spectra that is obtained as the cosine transform of the auto-correlation. This estimate points to an inherent small-scale process and is of same the order of magnitude as the Taylor microscale ($\lambda_T^+ \approx 80$–300 in the outer region at this particular Reynolds number). Phillips (1972) suggested that the microconvolutions of the interface are of the same scale as the interface thickness. We find support for this in the fact that the length scale derived from the normal velocity fluctuations over the microconvolutions in our data is of the same order as the interface thickness inferred as the vorticity thickness. Our analysis which is based on the normal velocity at the interface is consistent with the two-point correlation analysis of Westerweel *et al.* (2005) based on the axial velocity, who also concluded that integral length scales derived from the velocity information at the interface is close to the Taylor microscale.

The fluctuating characteristic of instantaneous $\tilde{U}_n$ at the interface is not apparent when the flow field is examined visually (for example in figure 2). Visual examination of the interface over the velocity field more strikingly gives an impression of its organization, i.e. the presence of small-scale contortions over large-scale bulges and valleys. It then follows that characterizing the large-scale behaviour of the interface would point to the length scale that governs this organization. A straightforward way is to observe the change in the interface height z_{i} that typically fluctuates between $\delta/3$ to δ with streamwise distance x. An example of the local interface height for the velocity field corresponding to figure 2(*b*) is shown in figure 8(*a*). The interface outline shows distinct large-scale variation in its local height with respect to the mean interface location ($Z_{\mathrm{i}} \approx 2\delta/3$). However, the interface often turns back on to itself and thus x is not a monotonic variable for $z_{\mathrm{i}}(x)$. This difficulty is overcome by characterizing the interface height with the distance s along the interface, i.e. $z_{\mathrm{i}}(s)$ as shown in figure 8(*b*). The abscissa in figure 8(*b*) is now monotonic. It should be noted that the horizontal axis in figure 8(*a*) and (*b*) are different but plotted on an equivalent scale. The trends of $z_{\mathrm{i}}(x)$ are clearly followed by $z_{\mathrm{i}}(s)$ at a proportional distance. For example, the sudden dip in $z_{\mathrm{i}}(x)$ (near $x/\delta \approx 1.6$) is accompanied by a similar dip in $z_{\mathrm{i}}(s)$ near $s/\delta \approx 3.25$. Similarly, the big bulge between $x/\delta \approx 0.5$ and $x/\delta \approx 1.3$ in figure 8(*a*) is also seen for $z_{\mathrm{i}}(s)$ at a proportional scale. The important aspect of figure 8(*a*) and (*b*) is that a single proportionality factor between s and x can be used to maintain all of the large-scale features of z_{i} and thereby permitting analysis of $z_{\mathrm{i}}(s)$. Here we perform auto-correlation of $z_{\mathrm{i}}(s)$. Figure 8(*c*) plots the auto-correlation $R_{z_{\mathrm{i}}z_{\mathrm{i}}}$ of the interface height along its distance obtained as an average from 1250 vector fields. The auto-correlation clearly indicates a large-scale feature which is expected from the visual examination. A characteristic length scale $\Lambda_x/\delta \approx 1.7$ is again obtained from peak location in the premultiplied spectra calculated from cosine transform of the auto-correlation in figure 8(*c*). In contrast to figure 7(*c*), the estimate of the integral length scale here is approximately two orders of magnitude higher. Figure 8(*c*) provides a direct validation of the assumption by Corrsin & Kistler (1955) that the mean interface thickness is much smaller than the radii of curvature of the interface. Although $\tilde{U}_n$ and z_{i} are not directly associated with the instantaneous entrainment rate, the two distinct length scales identified with help of these two quantities suggest that the dynamics at the

https://doi.org/10.1017/jfm.2013.641 Published online by Cambridge University Press

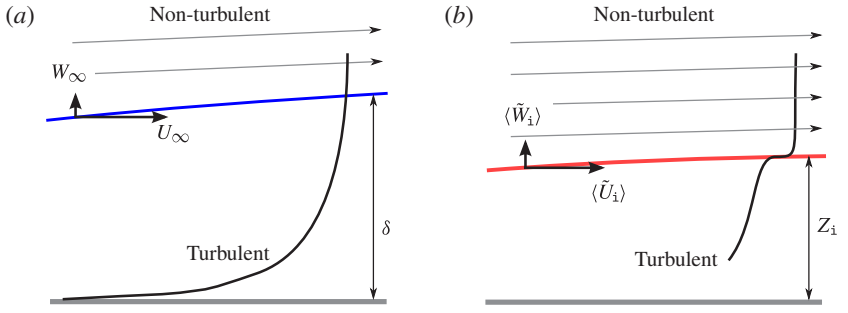


FIGURE 9. (Colour online) (*a*) Turbulent flow bounded by mean boundary-layer thickness δ. (*b*) Turbulent flow bounded by mean interface Z_i.

interface is likely to be a multiscale phenomena. These aspects will be explored in the following section, particularly for the mass flux.

7. Mass flux

We now look at the characteristics of mass flux, i.e. the instantaneous and mean entrainment across the interface.

7.1. *Average mass flux*

The mean turbulent boundary layer can be considered as a combination of an irrotational flow beyond the boundary-layer thickness δ, while the turbulence is confined below (see figure 9*a*). The free-stream velocities U_∞ and W_∞ at the boundary-layer edge contribute to the mean entrainment across the boundary (Head 1958). Therefore, the average mass flow rate per unit spanwise depth is

$$\mathrm{d}\dot{M} = \rho\,[U_\infty\,\mathrm{d}\delta - W_\infty\,\mathrm{d}x]. \tag{7.1}$$

The mass flux (rate of mass flow per unit area) is then given as

$$\frac{\mathrm{d}\dot{M}}{\mathrm{d}x} = \rho\left[U_\infty\frac{\mathrm{d}\delta}{\mathrm{d}x} - W_\infty\right] \tag{7.2}$$

$$= \rho\,U_\infty\left[\frac{\mathrm{d}\delta}{\mathrm{d}x} - \frac{\mathrm{d}\delta^*}{\mathrm{d}x}\right], \tag{7.3}$$

where δ^* is the displacement thickness and the streamwise growth of δ and δ^* is evaluated from appendix A using expressions (A 11) and (A 12), respectively. On substituting the experimental parameters we obtain $\mathrm{d}\dot{M}/\mathrm{d}x = 0.21$ kg m^{-2} s^{-1} from (7.3). Alternately the mean turbulent boundary layer can be considered as an irrotational flow that resides above the mean interface Z_i as shown in figure 9(*b*). The mean interface Z_i gradually grows with downstream x similar to the growth of δ. The entrainment mechanism within the interface would be then responsible for taking in the non-turbulent fluid to keep up with the momentum loss at the wall. The mean velocities at the interface $\langle \tilde{U}_i \rangle$ and $\langle \tilde{W}_i \rangle$ contribute to the mean entrainment across the interface. Therefore, the average mass flow rate per unit depth is

$$\mathrm{d}\dot{M} = \rho\,[\langle \tilde{U}_i \rangle\,\mathrm{d}Z_i - \langle \tilde{W}_i \rangle\,\mathrm{d}x]. \tag{7.4}$$

https://doi.org/10.1017/jfm.2013.641 Published online by Cambridge University Press

The mass flux (rate of mass flow per unit area) is

$$\frac{\mathrm{d}\dot{M}}{\mathrm{d}x} = \rho\left[\langle\tilde{U}_{\mathrm{i}}\rangle\frac{\mathrm{d}Z_{\mathrm{i}}}{\mathrm{d}x} - \langle\tilde{W}_{\mathrm{i}}\rangle\right] \tag{7.5}$$

$$\approx \rho\left[\langle\tilde{U}_{\mathrm{i}}\rangle\frac{Z_{\mathrm{i}}}{\delta}\frac{\mathrm{d}\delta}{\mathrm{d}x} - \langle\tilde{W}_{\mathrm{i}}\rangle\right]. \tag{7.6}$$

From figure 5, $\langle\tilde{U}_{\mathrm{i}}\rangle/U_\infty = 0.97$ and $\langle\tilde{W}_{\mathrm{i}}\rangle/U_\infty = -0.0025$. Substituting $Z_{\mathrm{i}}/\delta = 0.67$ from § 4 and $\mathrm{d}\delta/\mathrm{d}x$ from (A 11) we get $\mathrm{d}\dot{M}/\mathrm{d}x = 0.20$ kg m^{-2} s^{-1} from (7.6). A very good agreement is obtained between (7.3) and (7.6) indicating that the measurements are consistent with the theory in appendix A. Equivalence of (7.3) and (7.6) results in the following relationship between the mean velocity at the interface and the free-stream velocity:

$$U_\infty\left[\frac{\mathrm{d}\delta}{\mathrm{d}x} - \frac{\mathrm{d}\delta^*}{\mathrm{d}x}\right] \approx \left[\langle\tilde{U}_{\mathrm{i}}\rangle\frac{Z_{\mathrm{i}}}{\delta}\frac{\mathrm{d}\delta}{\mathrm{d}x} - \langle\tilde{W}_{\mathrm{i}}\rangle\right] \tag{7.7}$$

$$\therefore \quad \left[U_\infty - \langle\tilde{U}_{\mathrm{i}}\rangle\frac{Z_{\mathrm{i}}}{\delta}\right]\frac{\mathrm{d}\delta}{\mathrm{d}x} = W_\infty - \langle\tilde{W}_{\mathrm{i}}\rangle. \tag{7.8}$$

The ratio $Z_{\mathrm{i}}/\delta < 1$ and approaches a constant value of approximately 2/3 as noted in § 4. Equation (7.8) outlines approximate relations between the mean velocities at the interface and the free-stream velocities subject to constraint imposed by mass flux. Note that a similar expression for entrainment velocity exists for turbulent jets (Turner 1986). With some manipulation to (7.8) it can be shown that $\langle\tilde{W}_{\mathrm{i}}\rangle < 0$ and is $O(u_\tau)$.

7.2. *Instantaneous mass flux*

We have seen that the average interface velocities $\langle\tilde{U}_{\mathrm{i}}\rangle$ and $\langle\tilde{W}_{\mathrm{i}}\rangle$ give an accurate estimate of the 'average mass flux' through (7.6); this is the average entrainment across the boundary layer. However, instantaneously the mass flux entrained into the boundary layer via the interface depends on the 'entrainment velocity' (say, $\boldsymbol{v}_{\mathrm{E}}$, which is the difference between the fluid velocity and interface velocity), the density and the surface area (or in the present case interface line length):

$$\mathrm{d}\dot{m} = \rho\,\boldsymbol{v}_E\cdot\boldsymbol{n}\,\mathrm{d}s, \tag{7.9}$$

where $\mathrm{d}s$ is the interface line element, and the total mass flux is simply $\int \mathrm{d}\dot{m}$. Note that typically the entrainment velocities are of the order of Kolmogorov velocity scale (Holzner *et al.* 2007) and extremely difficult to measure directly. However, techniques such as high-speed PIV where the time evolution of the interface can be tracked to measure $\boldsymbol{v}_{\mathrm{i}}$ (interface velocity) with simultaneous measurement of $\tilde{U}_n$ may be suitable. To proceed further, it is simpler to consider a coordinate system moving with the free-stream velocity, such that $\boldsymbol{v} \equiv \boldsymbol{u} - \boldsymbol{U}_\infty$ and $\boldsymbol{U}_\infty = (U_\infty, 0, 0)$, and in this system the turbulent boundary layer grows outwards in time. Following Philip *et al.* (2014) and van Reeuwijk & Holzner (2014), appendix B shows that

$$\mathrm{d}\dot{m} \approx \frac{2\rho\nu}{K_0}\,v_j\,S_{ji}\,n_i\,\mathrm{d}s, \tag{7.10}$$

where S_{ij} is the strain-rate tensor and the quantities are evaluated on the interface. To identify the dominant length scales for mass entrainment, it is convenient to

https://doi.org/10.1017/jfm.2013.641 Published online by Cambridge University Press

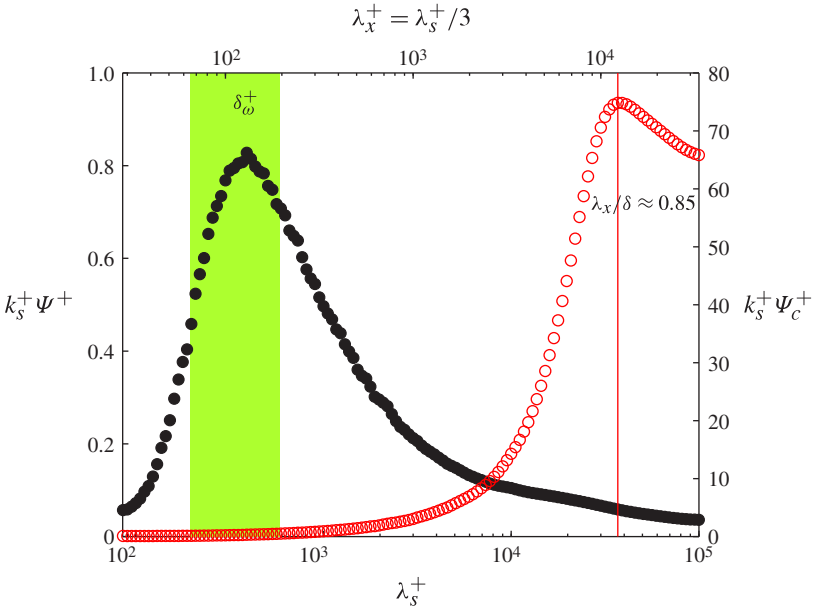


FIGURE 10. (Colour online) Premultiplied mass spectra: •, d$\dot{m}$; ○, $\dot{m}_c$. Shaded region indicates the extent over which the vorticity thickness ($\delta_\omega^+ = 195$) extends in s and x co-ordinate system at $Re_\tau = 14\,500$. Dashed-dotted line (shown in red online) indicates the peak in the spectra of $\dot{m}_c$ at $\lambda_x/\delta \approx 0.85$.

consider the two-point correlation of d$\dot{m}$ along the interface, s, or equivalently the spectra (the Fourier transform of the correlation function, Ψ). Figure 10 shows in filled symbols the premultiplied spectra ($k_s\Psi$) normalized by viscous scales as a function of wavelength along s, $\lambda_s = 2\pi/k_s$, averaged over 1250 images. In § 4 we found that the interface length is on an average three times longer than the unit streamwise distance, i.e. $\ell_s/L_x \approx 3$. Therefore, the equivalent streamwise wavelength $\lambda_x = \lambda_s/3$ is shown on the top axis of figure 10. The peak in the spectra suggests the scale at which the entrance of the mass appears most frequently. The peak seems to be close to the vorticity thickness (δ_ω^+) and not far from the Taylors microscale ($\lambda_T^+ \approx 80$ to 300 in the outer part of the boundary layer). The peak corresponds to the dominant length scale observed for the small-scale mechanisms that resemble nibbling. This is also consistent with observations in turbulent jets by da Silva & Taveira (2010), da Silva & dos Reis (2011) that $\delta_\omega \sim \lambda_T$. However, it is noted that since the measurements are limited in spatial resolution, the small-scale characteristic of d$\dot{m}$ in figure 10 should be regarded as a qualitative result emphasizing that the local scales are of the order of λ_T. Accordingly, the precise the numerical values are to be interpreted with caution.

To understand the large-scale entrainment mechanism we suggest considering the total or the cumulative mass entrained up to a particular distance s:

$$\dot{m}_c(s) = \int \mathrm{d}\dot{m} \approx \frac{2\rho\nu}{K_0} \int_{s'=0}^{s'=s} v_j\, S_{ji}\, n_i\, \mathrm{d}s'. \tag{7.11}$$

The rate of mass entrained between two points s_1 and s_2 along the interface is simply $\dot{m}_c(s_2) - \dot{m}_c(s_1)$. To characterize this difference in $\dot{m}_c(s)$, we turn to the analogous

https://doi.org/10.1017/jfm.2013.641 Published online by Cambridge University Press

structure function of velocity and the way it is used to characterize the dominant size of eddies (Davidson 2004). To this end we consider the second-order structure function of $\dot{m}_c(s)$, $\langle \Delta \dot{m}_c \rangle^2(r) \equiv \langle (\dot{m}_c(s+r) - \dot{m}_c(s))^2 \rangle$. Since the second-order structure function is algebraically related to the auto-correlation, to understand the dominant length scales in cumulative mass flux it is sufficient to look at the spectra of the function $\dot{m}_c(s)$. Figure 10 also shows in empty symbols the premultiplied spectra of the cumulative mass flux ($k_s \Psi_c$) normalized by viscous scales, the peak of which occurs at $\lambda_x/\delta \approx 0.85$. Therefore, motions of $O(\delta)$ cause the interface to be contorted and have large-scale indentations, which are responsible for organizing the small-scale nibbling phenomena over the interface. At the Reynolds number considered these scale estimates clearly demonstrate a wide separation of length scales that are present in the entrainment process.

Note that for the present case the total mass flux was calculated by two methods employing the average boundary-layer properties (cf. (7.3)) and the conditional profiles at the TNTI (cf. (7.6)). Ideally we should be able to calculate the total mass flux from (7.11); however, this turns out to be underestimated due to the resolution of the PIV data (see Philip *et al.* 2014 for a fuller discussion). Nonetheless, since our average interface is stationary (i.e. in the laboratory frame of reference the interface is steady on an average), the interface velocity on an average is zero, and we can estimate the total mass flux (per unit length) by ensemble averaging:

$$\frac{\rho}{\ell} \int_0^{\ell_s} \tilde{U}_n \, \mathrm{d}s, \tag{7.12}$$

where $\tilde{U}_n$ is the velocity normal to the interface, and ℓ_s is the total length of the interface for each image. The ensemble average of mass flux from 1250 images is 0.22 kg m^{-2} s^{-1}. This estimate of average mass flux is in acceptable agreement with those obtained from (7.3) and (7.6), which are 0.21 and 0.20 kg m^{-2} s^{-1}, respectively.

8. Summary and conclusions

Utilizing a unique experimental set-up and the HRNBLWT at University of Melbourne, we have documented the properties of the TNTI of a turbulent boundary layer at a relatively high Reynolds number. The Kármán number ($Re_\tau = 14\,500$) of the present experiments ensure that there is sufficient scale separation between the viscous scales (ν/u_τ) and the large scales of the flow of $O(\delta)$. The multicamera set-up achieves the magnification required to measure the smallest relevant scales ($\sim 6\eta$) while still able to measure structures as long as 2δ. This criteria is important to study any boundary-layer phenomena that has multiscale dynamics, entrainment being one of them. In comparison with previous experiments at similar high Reynolds numbers, the data acquired here provides a wealth of information over a large field of view with acceptable resolution for both large and small scales. A new approach based on the local kinetic energy is introduced to identify the TNTI. This approach and the criteria adopted detects the turbulent and non-turbulent zones in a two-dimensional velocity field effectively. The consistency of statistics validate the approach. As the kinetic energy criteria is based on velocity, it can be adopted for different measurement techniques and thereby one does not have to rely on passive markers to detect the TNTI. We have shown this for the hotwire data from the same facility and the collapse of intermittency profiles indicate a Reynolds number invariance over $Re_\tau = 2700$–$22\,000$. The mean location of the interface (Z_i) is at $2\delta/3$ while the standard deviation of its spread is $\delta/9$ approximately.

https://doi.org/10.1017/jfm.2013.641 Published online by Cambridge University Press

The two-dimensional interface outline is highly contorted and shows identifiable variations on both large and small scales. It has been previously shown that the TNTI exhibits fractal characteristics. However, here we have evidenced this fractal characteristic in a high-Reynolds-number turbulent boundary layer using only velocity measurements, in agreement with past observations. Adhering to its fractal nature, the interface outline also has a significantly longer length per unit streamwise distance. It is concluded that the fractal geometry increases the effective surface area of the turbulent flow that is exposed to the non-turbulent free stream and thereby the small-scale nibbling mechanism becomes consequential to the net entrainment at smaller scales.

Conditional analysis at the interface shows that there is a bulk motion associated with large variations in the local interface height, i.e. the potential flow adjusts to the instantaneous thickness of the turbulent flow. The local interface height spans two-thirds of the upper boundary layer and appears in the form of large bulges/valleys. The conditional averages shown in figure 5 with interface height as a reference clearly establish the presence of a superlayer, first proposed by Corrsin & Kistler (1955), in a turbulent boundary layer. The superlayer is characterized by a shear-layer-like profile for the streamwise momentum. Also a discontinuity in the spanwise vorticity and a sudden rise in the Reynolds shear stress on the turbulent side is observed at the interface. The width of the interface layer is deduced as 195 viscous units, equivalent to the wall-normal distance over which the jump in streamwise velocity and discontinuity in spanwise vorticity occurs. The examination of the superlayer jump condition of Reynolds (1972) over this width shows good agreement between the experiment and theory. Similar characteristics of the superlayer have been observed Westerweel *et al.* (2005) in jets and Bisset *et al.* (2002) in wakes.

Figures 3(*c*) and (*d*) point to the fractal nature of the interface and sets the stage to examine the dynamics at the interface in a multiscale sense. It suggests that the length scales on the either extremes of the data in figure 3(*c*), where the fractal characteristic fails to appear, may correspond to two different mechanisms. These two mechanism occur simultaneously however with different outcomes as shown in § 7. It is noted that the fractal nature of scales that are $O(\delta)$ is debatable in the absence of converged statistics. We have examined the dominant length scales at the interface and those are that important to the entrainment. The auto-correlation of the normal velocity at the interface reveals a characteristic scale that is much smaller than the boundary-layer thickness δ. Since the small-scale contortions of the interface geometry dictate the direction of the normal vector (and, thus, the direction and magnitude of $\tilde{U}_n$), the length scale from the auto-correlation is the order of the scale of the contortion. On the other hand, the large-scale organization of the interface is revealed by considering the auto-correlation of the local interface height along the interface length s. The large-scale organization of the interface in the form of appearance of bulges and valleys can be either an outcome of local instability at the interface (Townsend 1966) or motions triggered by the near-wall turbulence (Kovasznay 1970). In either case a large-scale bulge/valley influences the flow in the turbulent and the non-turbulent region in its vicinity (see figure 4*c*). The large-scale behaviour of the interface height is of $O(\delta)$ and points to the upper extent of motions that influences the TNTI dynamics in boundary layers. Further in this study a novel approach of examining the mass flux is presented. The average mass flux (mean entrainment) is calculated from the classical boundary-layer growth equation and found to be in excellent agreement with a newly formulated growth equation of the mean interface that consists of the conditional velocity statistics. We further demonstrate that the

https://doi.org/10.1017/jfm.2013.641 Published online by Cambridge University Press

instantaneous mass flux over an interface outline has a high-frequency behaviour. This high-frequency behaviour is indicative of small-eddy motions residing in the superlayer and resembles nibbling. The cumulative mass flux on the other hand is found to account for bulk entrainment over the large-scale bulges/valleys of the interface. It is found that the small-scale phenomenon has an approximate streamwise extent that is of the same order as the Taylor microscale in the flow. This observation is in agreement with the previous studies made in jets (Westerweel *et al.* 2009; da Silva & Taveira 2010) and wakes (Bisset *et al.* 2002). As remarked by da Silva & dos Reis (2011) such TNTI behaviour is a characteristic of flows with mean shear. The small-scale processes of entrainment appear to be statistically independent of the large-scale motions that convolute the interface (Phillips 1972). This estimate is also consistent with the determined width of the superlayer within which spanwise vorticity is concentrated in the form of nibbling motions. The large-scales over which significant non-turbulent momentum is entrained are found to be $O(\delta)$. This estimate is of the scale on which the bulges/valleys are organized. We have seen that both the large contortions and small wrinkles in the interface outline contribute towards the increased surface area of a two-dimensional interface. The instantaneous entrainment rate is enhanced by the abundance of small scales residing on the two-dimensional TNTI. It is inferred that the large scales govern the overall rate of entrainment and the small-scale eddy motions reside on the large-scale features, organized in a manner to keep the aggregate entrainment consistent with the boundary-layer growth. Subsequently the small-scale motions convert the non-turbulent flow to a turbulent state by vorticity transfer through diffusion.

Acknowledgements

The authors wish to acknowledge the financial support of the Australian Research Council. Professor C. Meneveau is thanked for stimulating discussions and helpful comments on the instantaneous mass-flux analysis.

Appendix A. Evaluation of x derivative of δ and δ^*

The streamwise evolution of a zero-pressure-gradient turbulent boundary layer can be evaluated by integrating the Kármán integral momentum equation to obtain $Re_x(Re_\theta)$:

$$\frac{\mathrm{d}\theta}{\mathrm{d}x} = \frac{\mathrm{d}Re_\theta}{\mathrm{d}Re_x} = \frac{u_\tau^2}{U_\infty^2}. \tag{A 1}$$

This can be applied to establish some preliminary identities and subsequently x derivatives of quantities of interest. We start with the Rotta–Clauser skin–friction relation, $U_\infty^+(Re_{\delta^*})$ (Monkewitz, Chauhan & Nagib 2007):

$$U_\infty^+ = \frac{1}{\kappa}\ln Re_{\delta^*} + C, \quad \kappa = 0.384, \quad C = 3.3. \tag{A 2}$$

$$\therefore \quad \frac{\mathrm{d}U_\infty^+}{\mathrm{d}Re_{\delta^*}} = \frac{1}{\kappa Re_{\delta^*}}. \tag{A 3}$$

From the definition of the shape factor H,

$$H = \frac{1}{1 - I_{WW}/U_\infty^+} \quad \Rightarrow \quad \frac{\mathrm{d}H}{\mathrm{d}Re_{\delta^*}} = \frac{\mathrm{d}H}{\mathrm{d}U_\infty^+}\frac{\mathrm{d}U_\infty^+}{\mathrm{d}Re_{\delta^*}}. \tag{A 4}$$

https://doi.org/10.1017/jfm.2013.641 Published online by Cambridge University Press

For the classical logarithmic theory, $I_{WW} = \int_0^\infty (U_\infty^+ - U^+)^2 \mathrm{d}(z/\Delta)$ asymptotes to a constant very quickly which is evident in the experimental data (Monkewitz *et al.* 2007); i.e. $I_{WW} = 7.11$:

$$\therefore \quad \frac{\mathrm{d}H}{\mathrm{d}Re_{\delta^*}} = -\frac{H^2 I_{WW}}{(U_\infty^+)^2} \frac{1}{\kappa Re_{\delta^*}}. \tag{A 5}$$

Further,

$$H = \frac{Re_{\delta^*}}{Re_\theta} \quad \Rightarrow \quad \frac{\mathrm{d}H}{\mathrm{d}Re_{\delta^*}} = \frac{1}{Re_\theta} - \frac{H}{Re_\theta} \frac{\mathrm{d}Re_\theta}{\mathrm{d}Re_{\delta^*}}. \tag{A 6}$$

$$\therefore \quad \frac{\mathrm{d}Re_{\delta^*}}{\mathrm{d}Re_\theta} = \frac{H}{1 + \dfrac{H I_{WW}}{\kappa (U_\infty^+)^2}}. \tag{A 7}$$

Next, we look at the streamwise development of the Rotta–Clauser thickness $\Delta (= \delta^* U_\infty / u_\tau)$ and arrive at the following useful results:

$$\frac{\mathrm{d}\Delta}{\mathrm{d}x} = \frac{\mathrm{d}(Re_{\delta^*} U_\infty^+)}{\mathrm{d}Re_x} = \frac{\mathrm{d}Re_{\delta^*}}{\mathrm{d}Re_\theta} \frac{\mathrm{d}Re_\theta}{\mathrm{d}Re_x} \frac{\mathrm{d}(Re_{\delta^*} U_\infty^+)}{\mathrm{d}Re_{\delta^*}} \tag{A 8}$$

$$= \frac{H}{1 + \dfrac{H I_{WW}}{\kappa (U_\infty^+)^2}} \frac{1}{(U_\infty^+)^2} \left(U_\infty^+ + \frac{1}{\kappa} \right) \tag{A 9}$$

$$\therefore \quad \frac{\mathrm{d}\Delta}{\mathrm{d}x} = \frac{H (\kappa U_\infty^+ + 1)}{H I_{WW} + \kappa (U_\infty^+)^2}. \tag{A 10}$$

In a zero-pressure-gradient turbulent boundary layer the ratio Δ/δ asymptotes to a constant at high Reynolds numbers (Chauhan *et al.* 2009). Thereby, $\mathrm{d}\delta/\mathrm{d}x$ can be evaluated as

$$\frac{\mathrm{d}\delta}{\mathrm{d}x} = \frac{\delta^+}{Re_{\delta^*}} \frac{\mathrm{d}\Delta}{\mathrm{d}x}. \tag{A 11}$$

Utilizing the definition of Δ we can also write

$$\frac{\mathrm{d}\delta^*}{\mathrm{d}x} = \frac{1}{U_\infty^+} \left[\frac{\mathrm{d}\Delta}{\mathrm{d}x} + \frac{\Delta}{u_\tau} \frac{\mathrm{d}u_\tau}{\mathrm{d}x} \right]. \tag{A 12}$$

The term with x derivative of u_τ is expressed as

$$\frac{\Delta}{u_\tau} \frac{\mathrm{d}u_\tau}{\mathrm{d}x} = \Delta \left(-\frac{1}{U_\infty^+} \frac{\mathrm{d}U_\infty^+}{\mathrm{d}x} \right) \tag{A 13}$$

$$= -Re_{\delta^*} \frac{\mathrm{d}Re_\theta}{\mathrm{d}Re_x} \frac{\mathrm{d}Re_{\delta^*}}{\mathrm{d}Re_\theta} \frac{\mathrm{d}U_\infty^+}{\mathrm{d}Re_{\delta^*}} \tag{A 14}$$

$$= -Re_{\delta^*} \frac{H}{1 + \dfrac{H I_{WW}}{\kappa (U_\infty^+)^2}} \frac{1}{(U_\infty^+)^2} \frac{1}{\kappa Re_{\delta^*}}. \tag{A 15}$$

$$\therefore \quad \frac{\Delta}{u_\tau} \frac{\mathrm{d}u_\tau}{\mathrm{d}x} = -\frac{H}{H I_{WW} + \kappa (U_\infty^+)^2}. \tag{A 16}$$

We can now evaluate the streamwise growth rate of δ and δ^* by utilizing (A 10) and (A 16) in (A 11) and (A 12).

https://doi.org/10.1017/jfm.2013.641 Published online by Cambridge University Press

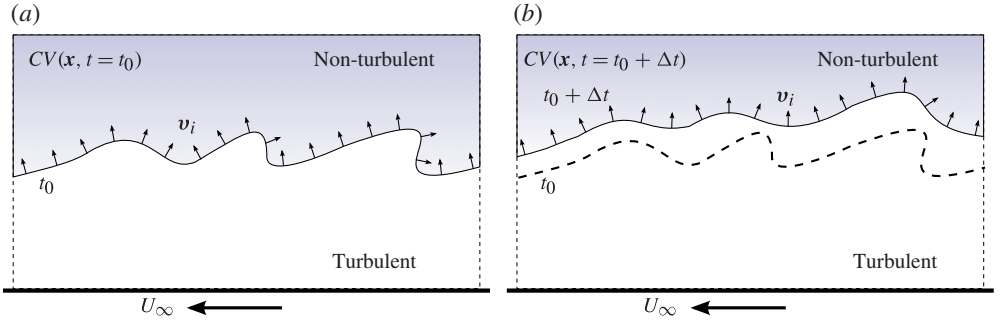


FIGURE 11. (Colour online) Turbulent boundary layer in a reference frame where wall is moving at U_∞. The non-turbulent control volume $CV(\boldsymbol{x}, t)$ changes with time t. (*a*) At time $t = t_o$, $CV(\boldsymbol{x}, t = t_o)$. (*b*) At time $t = t_0 + \Delta t$, $CV(\boldsymbol{x}, t = t_o + \Delta t)$. The interface is shown to move with a velocity $\boldsymbol{v}_I$.

Appendix B. Turbulent entrainment into a non-turbulent volume

Here we follow the analysis of Philip *et al.* (2014) where an expression for the 'entrainment velocity' (to be defined below) is derived based on an isokinetic energy TNTI. A similar analysis has also been carried out by van Reeuwijk & Holzner (2014), however using an isovorticity TNTI. The purpose of this appendix is to provide a self-contained treatment of the 'entrainment velocity' for the sake of completeness, which will be employed to investigate the dominant length scales present during the mass entrainment.

We employ a coordinate system moving with the free-stream velocity U_∞, such that the kinetic energy, $K = (1/2)(\boldsymbol{v} \cdot \boldsymbol{v})$, where $\boldsymbol{v} \equiv \boldsymbol{u} - \boldsymbol{U}_\infty$ and $\boldsymbol{U}_\infty = (U_\infty, 0, 0)$. The evolution equation for K is

$$\frac{\partial K}{\partial t} + \frac{\partial}{\partial x_i}(v_i K) = \frac{\partial}{\partial x_i}\left(-v_j \frac{p}{\rho}\delta_{ij} + v_j 2\nu S_{ji}\right) - 2\nu S_{ji}\frac{\partial v_j}{\partial x_i}, \tag{B 1}$$

where $S_{ij} = (1/2)(\partial v_i/\partial x_j + \partial v_j/\partial x_i)$. Now consider the non-turbulent control volume (CV) shown as a shaded region in figure 11 which is changing in time with the moving interface. On integrating (B 1) over a control volume in the non-turbulent (and almost irrotational, see figure 11) region $CV(\boldsymbol{x}, t)$ and subsequently employing the Leibniz–Reynolds integral rule, one obtains

$$\frac{\mathrm{d}\mathscr{K}_{CV}}{\mathrm{d}t} = \int_S K(v_i - v_{Ii})n_i, \mathrm{d}S + \int_S \left(v_j \frac{p}{\rho}\delta_{ij} - v_j 2\nu S_{ji}\right) n_i \,\mathrm{d}S - D. \tag{B 2}$$

Here, the normal vector $\boldsymbol{n} = -\nabla K/|\nabla K|_{K=K_0}$ is pointing into the CV (K_0 is the threshold used for detecting the interface), $S(\boldsymbol{x}, t)$ is the surface enclosing CV, $\boldsymbol{v}_I$ is the velocity of the surface or the interface, $\mathscr{K}_{CV} \equiv \int_{CV(\boldsymbol{x},t)} K \,\mathrm{d}V$, and D is the dissipation inside $CV(\boldsymbol{x}, t)$. Now, the local entrainment velocity is the difference of the interface velocity and the fluid velocity $\boldsymbol{v}_\mathrm{E} \equiv \boldsymbol{v}_I - \boldsymbol{v}$. As shown in Philip *et al.* (2014), equation (B 2) reduces to

$$\int_{S_I} \boldsymbol{v}_\mathrm{E} \cdot \boldsymbol{n} \,\mathrm{d}S \approx \frac{\Phi_\nu}{K_0}, \tag{B 3}$$

where $\Phi_\nu \equiv \int_{S_I} 2\nu v_j S_{ji} n_i \,\mathrm{d}S$, and similarly its two-dimensional equivalent Φ_ν^{2D} can be defined with $i, j = 1, 3$ for the present purpose where we have velocity fields on only two-dimensional PIV planes.

https://doi.org/10.1017/jfm.2013.641 Published online by Cambridge University Press

REFERENCES

ADRIAN, R. J. 2007 Hairpin vortex organization in wall turbulence. *Phys. Fluids* **19**, 041301.

ANAND, R., BOERSMA, B. J. & AGRAWAL, A. 2009 Detection of turbulent/non-turbulent interface for an axisymmetric turbulent jet: evaluation of known criteria and proposal of a new criterion. *Exp. Fluids* **47** (6), 995–1007.

ANTONIA, R. A. 1972 Conditionally sampled measurements near the outer edge of a turbulent boundary layer. *J. Fluid Mech.* **56** (1), 1–18.

BISSET, D. K., HUNT, J. C. R. & ROGERS, M. M. 2002 The turbulent/non-turbulent interface bounding a far wake. *J. Fluid Mech.* **451**, 383–410.

BROWN, G. L. & ROSHKO, A. 1974 On density effects and large structure in turbulent mixing layers. *J. Fluid Mech.* **64**, 775–816.

CANNON, S., CHAMPAGNE, E. & GLEZER, A. 1993 Observations of large-scale structures in wakes behind axisymmetric bodies. *Exp. Fluids* **14**, 447–450.

CHAUHAN, K. A., MONKEWITZ, P. A. & NAGIB, H. M. 2009 Criteria for assessing experiments in zero pressure gradient boundary layers. *Fluid Dyn. Res.* **41**, 021404.

CHEN, C.-H. P. & BLACKWELDER, R. F. 1978 Large-scale motion in a turbulent boundary layer: a study using temperature contamination. *J. Fluid Mech.* **89**, 1–31.

COLES, D. E. & HIRST, E. A. 1968 Computation of turbulent boundary layers. In *Proceedings of AFOSR-IFP Stanford Conference,* vol. 2 .

CORRSIN, S. & KISTLER, A. L. 1955 Free-stream boundaries of turbulent flows. *Tech. Rep*. TN-1244. NACA, Washington, DC.

DA SILVA, C. B. & DOS REIS, R. J. N. 2011 The role of coherent vortices near the turbulent/non-turbulent interface in a planar jet. *Phil. Trans. R. Soc. Lond.* A *Math. Phys. Sci.* **369**, 738–753.

DA SILVA, C. B. & PEREIRA, J. C. F. 2008 Invariants of the velocity-gradient, rate-of-strain, and rate-of-rotation tensors across the turbulent/nonturbulent interface in jets. *Phys. Fluids* **20** (5), 055101.

DA SILVA, C. B. & TAVEIRA, R. R. 2010 The thickness of the turbulent/nonturbulent interface is equal to the radius of the large vorticity structures near the edge of the shear layer. *Phys. Fluids* **22**, 121702.

DAVIDSON, P. A. 2004 *Turbulence: An Introduction for Scientists and Engineers*. Oxford University Press.

DE SILVA, C. M., CHAUHAN, K. A., ATKINSON, C. H., BUCHMANN, N. A., HUTCHINS, N., SORIA, J. & MARUSIC, I. 2012 Implementation of large-scale PIV measurements for wall bounded turbulence at high Reynolds numbers. In *Proceedings of 18th Australasian Fluid Mechanics Conference, 3–7 December*, Launceston, Australia.

DE SILVA, C. M., PHILIP, J., CHAUHAN, K., MENEVEAU, C. & MARUSIC, I. 2013 Multiscale geometry and scaling of the turbulent-nonturbulent interface in high Reynolds number boundary layers. *Phys. Rev. Lett.* **111**, 044501.

FACKRELL, J. E. & ROBINS, A. G. 1982 Concentration fluctuations and fluxes in plumes from point sources in a turbulent boundary layer. *J. Fluid Mech.* **117**, 1–26.

FIEDLER, H. & HEAD, M. R. 1966 Intermittency measurements in the turbulent boundary layer. *J. Fluid Mech.* **25**, 719–735.

HANCOCK, P. E. & BRADSHAW, P. 1989 Turbulence structure of a boundary layer beneath a turbulent free stream. *J. Fluid Mech.* **205**, 45–76.

HART, D. P. 2000 PIV error correction. *Exp. Fluids* **29** (1), 13–22.

HEAD, M. R. 1958 Entrainment in the turbulent boundary layer. *Aero. Res. Counc. Rep* 3152.

HEDLEY, T. B. & KEFFER, J. F. 1974*a* Some turbulent/non-turbulent properties of the outer intermittent region of a boundary layer. *J. Fluid Mech.* **64**, 645–678.

HEDLEY, T. B. & KEFFER, J. F. 1974*b* Turbulent/non-turbulent decisions in an intermittent flow. *J. Fluid Mech.* **64**, 625–644.

HOLZNER, M., LIBERZON, A., NIKITIN, N., KINZELBACH, W. & TSINOBER, A. 2007 Small-scale aspects of flows in proximity of the turbulent/nonturbulent interface. *Phys. Fluids* **19**, 071702.

HOLZNER, M. & LÜTHI, B. 2011 Laminar superlayer at the turbulence boundary. *Phys. Rev. Lett.* **106**, 134503.

https://doi.org/10.1017/jfm.2013.641 Published online by Cambridge University Press

HUNT, J. C. R. 1994 Atmospheric jets and plumes. In *Recent Research Advances in the Fluid Mechanics of Turbulent Jets and Plumes* (ed. P. Davies & M. J. V. Neves), pp. 309–334. Kluwer.

HUNT, J. C. R., ROTTMAN, J. W. & BRITTER, R. E. 1984 Some physical processes involved in the dispersion of dense gases. In *Proceedings of IUTAM Symposium 'Atmospheric Dispersion of Heavy Gases and Small Particles'* (ed. G. Ooms & H. Tennekes), pp. 361–395. Springer.

HUTCHINS, N., NICKELS, T. B., MARUSIC, I. & CHONG, M. S. 2009 Hot-wire spatial resolution issues in wall-bounded turbulence. *J. Fluid Mech.* **635**, 103–136.

ISHIHARA, T., HUNT, J. C. R. & KANEDA, Y. 2012 Intense dissipative mechanisms of strong thin shear layers in high Reynolds number turbulence. *Bull. Am. Phys. Soc.* **57** (17), A23.00004.

JIMÉNEZ, J., HOYAS, S., SIMENS, M. P. & MIZUNO, Y. 2010 Turbulent boundary layers and channels at moderate Reynolds number. *J. Fluid Mech.* **657**, 335–360.

KHASHEHCHI, M., OOI, A., SORIA, J. & MARUSIC, I. 2013 Evolution of the turbulent/non-turbulent interface of an axisymmetric turbulent jet. *Exp. Fluids* **54** (1), 1–12.

KOVASZNAY, L. S. G. 1967 Structure of the turbulent boundary layer. *Phys. Fluids Suppl.* **10**, S25–S30.

KOVASZNAY, L. S. G. 1970 The turbulent boundary layer. *Annu. Rev. Fluid Mech.* **2**, 95–112.

KOVASZNAY, L. S. G., KIBENS, V. & BLACKWELDER, R. F. 1970 Large-scale motion in the intermittent region of a turbulent boundary layer. *J. Fluid Mech.* **41**, 283–325.

KULANDAIVELU, V. 2012 Evolution of zero pressure gradient turbulent boundary layers from different initial conditions. PhD thesis, The University of Melbourne, Melbourne, Australia.

MARUSIC, I. & KUNKEL, G. J. 2003 Streamwise turbulence intensity formulation for flat-plate boundary layers. *Phys. Fluids* **15**, 2461–2464.

MATHEW, J. & BASU, A. J. 2002 Some characteristics of entrainment at a cylindrical turbulence boundary. *Phys. Fluids* **14**, 2065–2072.

MENEVEAU, C. & SREENIVASAN, K. R. 1990 Interface dimension in intermittent turbulence. *Phys. Rev.* A **41** (4), 2246–2248.

MONKEWITZ, P. A., CHAUHAN, K. A. & NAGIB, H. M. 2007 Self-consistent high-Reynolds-number asymptotics for zero-pressure-gradient turbulent boundary layers. *Phys. Fluids* **19**, 115101.

NYCHAS, S. G., HERSHEY, H. C. & BRODKEY, R. S. 1973 A visual study of turbulent shear flow. *J. Fluid Mech.* **61**, 513–540.

PAIZIS, S. T. & SCHWARZ, W. H. 1974 An investigation of the topography and motion of the turbulent interface. *J. Fluid Mech.* **63** (2), 315–343.

PHILIP, J. & MARUSIC, I. 2012 Large-scale eddies and their role in entrainment in turbulent jets and wakes. *Phys. Fluids* **24**, 055108.

PHILIP, J., MENEVEAU, C., DE SILVA, C. M. & MARUSIC, I. 2014 Multiscale analysis of fluxes at the turbulent/non-turbulent interface in high Reynolds number boundary layers. *Phys. Fluids* **26**, 015105.

PHILLIPS, O. M. 1972 The entrainment interface. *J. Fluid Mech.* **51**, 97–118.

PRASAD, R. R. & SREENIVASAN, K. R. 1989 Scalar interfaces in digital images of turbulent flows. *Exp. Fluids* **7** (4), 259–264.

REYNOLDS, W. C. 1972 Large-scale instabilities of turbulent wakes. *J. Fluid Mech.* **54**, 481–488.

SANDHAM, N. D., MUNGAL, M. G., BROADWELL, J. E. & REYNOLDS, W. C. 1988 Scalar entrainment in the mixing layer. In *Proceedings of the Summer Program, CTR - Stanford* pp. 69–76.

SCHNEIDER, W. 1981 Flow induced by jets and plumes. *J. Fluid Mech.* **108** (1), 55–65.

SEMIN, N. V., GOLUB, V. V., ELSINGA, G. E. & WESTERWEEL, J. 2011 Laminar superlayer in a turbulent boundary layer. *Tech. Phys. Lett.* **37** (12), 1154–1157.

SREENIVASAN, K. R. 1991 Fractals and multifractals in fluid turbulence. *Annu. Rev. Fluid Mech.* **23** (1), 539–604.

SREENIVASAN, K. R. & MENEVEAU, C. 1986 The fractal facets of turbulence. *J. Fluid Mech.* **173**, 357–386.

SREENIVASAN, K. R., RAMSHANKAR, R. & MENEVEAU, C. 1989 Mixing, entrainment and fractal dimensions of surfaces in turbulent flows. *Phil. Trans. R. Soc. Lond.* A *Math. Phys. Sci.* **421** (1860), 79–108.

https://doi.org/10.1017/jfm.2013.641 Published online by Cambridge University Press

TAYLOR, G. I. 1921 Diffusion by continuous movements. *Proc. Lond. Math. Soc.* **20**, 196–211.

TAYLOR, G. I. 1958 Flow induced by jets. *J. Aerosp. Sci.* **25**, 464–465.

THOMPSON, B. G. J. 1964 A critical review of existing methods of calculating the turbulent boundary layer. *Aero. Res. Counc. Rep* 3447.

TOWNSEND, A. A. 1966 The mechanism of entrainment in free turbulent flows. *J. Fluid Mech.* **26**, 689–715.

TOWNSEND, A. A. 1976 *The Structure of Turbulent Shear Flow*. Cambridge University Press.

TURNER, J. S. 1986 Turbulent entrainment: the development of the entrainment assumption, and its application to geophysical flows. *J. Fluid Mech.* **173**, 431–471.

VAN REEUWIJK, M. & HOLZNER, M. 2014 The turbulence boundary of a temporal jet.. *J. Fluid Mech.* **739**, 254–275.

WESTERWEEL, J., FUKUSHIMA, C., PEDERSEN, J. M. & HUNT, J. C. R. 2005 Mechanics of the turbulent-nonturbulent interface of a jet. *Phys. Rev. Lett.* **95**, 174501.

WESTERWEEL, J., FUKUSHIMA, C., PEDERSEN, J. M. & HUNT, J. C. R. 2009 Momentum and scalar transport at the turbulent/non-turbulent interface of a jet. *J. Fluid Mech.* **631**, 199–230.

https://doi.org/10.1017/jfm.2013.641 Published online by Cambridge University Press